No Transition Disk? Infrared Excess, PAH, H_2, and X-rays from the Weak-Lined T Tauri Star DoAr 21

Eric L. N. Jensen[1], David H. Cohen[1], Marc Gagné[2]

ABSTRACT

As part of a program to understand disk dispersal and the interplay between circumstellar disks and X-ray emission, we present new high-resolution mid-infrared imaging, high-resolution optical spectroscopy, and *Chandra* grating X-ray spectroscopy of the weak-lined T Tauri star DoAr 21. DoAr 21 is a strong X-ray emitter, with conflicting evidence in the literature about its disk properties. It shows weak $H\alpha$ emission (reported here for the first time since the 1950s); polarimetric variability; PAH and H_2 emission; and a strong, spatially-resolved 24-μm excess in archival *Spitzer* photometry. Gemini sub-arcsecond-resolution 9–18 μm images show that there is little or no excess mid-infrared emission within 100 AU of the star; the excess emission is extended over several arcseconds and is quite asymmetric. The extended emission is bright in the UV-excited $\lambda = 11.3$ μm PAH emission feature. A new high-resolution X-ray grating spectrum from *Chandra* shows that the stellar X-ray emission is very hard and dominated by continuum emission; it is well-fit by a multi-temperature thermal model, typical of hard coronal sources. We argue that the far-ultraviolet emission from the transition region is sufficient to excite the observed extended PAH and continuum emission, and that the H_2 emission may be similarly extended and excited. While this extended emission may be a disk in the final stages of clearing, it also could be more akin to a small-scale photodissociation region than a protoplanetary disk, highlighting both the very young ages ($< 10^6$ yr) at which some stars are found without disks, and the extreme radiation environment around even late-type pre–main-sequence stars.

---

[1]Swarthmore College Department of Physics and Astronomy, 500 College Ave., Swarthmore, PA 19081. E-mail ejensen1, dcohen1@swarthmore.edu.

[2]West Chester University Department of Geology and Astronomy, West Chester, PA 19383

Subject headings: circumstellar matter — stars: planetary systems: protoplanetary disks — stars: coronae — stars: individual (DoAr 21) — stars: pre-main sequence — X-rays: stars

1. Introduction

An open question in early stellar evolution and planet formation is the process and timescale by which stars disperse their protoplanetary disks. Central to this question is the lifetime of the gas component of circumstellar disks. The gas dominates the disk mass, but since small dust grains dominate the infrared opacity, dispersal or growth of these grains can significantly reduce or eliminate the excess infrared emission that is often taken to be the primary signature of a circumstellar disk, even if substantial gas is still present.

Related to the question of gas disk survival and evolution is the influence of X-ray emission on the circumstellar gas, and vice versa. T Tauri stars, low-mass pre–main-sequence stars, are often strong X-ray emitters (see, e.g., the review of Feigelson & Montmerle 1999, and references therein). A detailed understanding of the X-ray emission from these young stars is important both for an understanding of the early evolution of the stars themselves, and due to the X-rays' impact on the surrounding environment. T Tauri stars are often surrounded by disks of gas and dust, from which planets presumably form later in the pre–main-sequence phase. The physical state of these disks is strongly influenced by the star's X-ray emission. The X-rays are the dominant source of ionization of the disk (Igea & Glassgold 1999) and they strongly influence the disk chemistry (Maloney et al. 1996). X-ray flares from the young Sun may have produced the isotopic anomalies seen today in meteorites (Feigelson, Garmire, & Pravdo 2002).

Similarly, the presence of circumstellar gas may play a role in shaping or modifying the star's X-ray emission. The models most often proposed for the X-ray emission of T Tauri stars are, broadly, solar-type magnetic activity scaled up by rapid rotation and/or longer convective turnover times; and interaction between a stellar magnetic field and a circumstellar disk, perhaps via accretion. However, neither the details of the magnetic field geometry nor where exactly the X-rays are produced is well established observationally (e.g., Feigelson & Montmerle 1999). The unprecedented X-ray spectral resolution and sensitivity of the *Chandra* X-ray satellite offers an opportunity to place much better constraints on the temperature and density of the X-ray emitting gas, thereby providing potentially important information about the X-ray emission mechanism(s), and about the X-ray radiation field

incident on the circumstellar disk.

To date, however, only a modest number of high-spectral-resolution X-ray observations of pre–main-sequence stars have been published; even the distances to the nearest star-forming regions result in X-ray fluxes that make high-resolution observations prohibitively long. There are a handful of notable exceptions, however. TW Hya (Kastner et al. 2002) and HD 98800 (Kastner et al. 2004) both lie in the nearby TW Hya association, with a distance of roughly 50 pc and an age of 5–15 Myr (Weintraub et al. 2000, and references therein). The *Chandra* X-ray spectrum of TW Hya yielded a surprisingly low temperature for the X-ray emitting gas, and suggestions of very high densities in the X-ray emitting regions, leading Kastner et al. (2002) to suggest that the X-ray emission is related to accretion from the star's circumstellar disk. Stelzer & Schmitt (2004) reached a similar conclusion based on density diagnostics in TW Hya's XMM-Newton spectrum, and also attributed the low Fe abundance seen in the X-ray emitting gas to depletion of some elements from the gas phase onto dust grains in the disk. Schmitt et al. (2005) presented similar evidence for high-density X-ray emitting gas around the classical T Tauri star BP Tau.

In contrast, the X-ray spectra of both HD 98800 (Kastner et al. 2004) and the similarly-aged (~ 10 Myr) PZ Tel (Argiroffi et al. 2004) are quite similar to spectra of older solar-type stars, suggesting that their X-ray activity is, to first order, scaled-up solar activity. Solar-like X-ray activity is also seen in AB Dor (Sanz-Forcada, Maggio, & Micela 2003), which is near or recently arrived on the zero-age main sequence. Notably, TW Hya and BP Tau show clear evidence of active accretion from their circumstellar disks, while the stars with more solar-like X-ray emission do not have disks.[1]

In the context both of understanding disk evolution and of understand the interplay between disks and X-rays, the weak-lined T Tauri star DoAr 21 (a.k.a. V2246 Oph, Elias 2-14, VSSG 23, GSS 23, ROXs 8, Haro 1-6, YLW 26, HBC 637, ROXR1 13) presents an interesting case study. It has no strong evidence for accretion or a massive disk, and yet it is one of the few T Tauri stars around which emission from H_2 and PAH molecules has been detected (Sec. 2.2). Bary et al. (2002) suggest that it may retain a gas-only disk in which all of the dust has coagulated into larger grains; Cieza et al. (2008) classify it as a "transition disk," one in the process of being cleared from the inside out. In addition, it is the most luminous X-ray source in ρ Oph, making it an excellent laboratory to study the influence of X-rays and circumstellar material.

---

[1]Only the southern component (HD 98800 B) of the wide binary pair in HD 98800 has circumstellar material (Koerner et al. 2000), while Kastner et al. (2004) show clearly that the X-ray spectrum they detect and analyze is from the diskless northern component, HD 98800 A.

Here we present new Gemini mid-infrared images and *Chandra* high-resolution grating spectra of DoAr 21. The primary contrast of DoAr 21 with the handful of pre–main-sequence stars previously observed at high X-ray spectral resolution is the combination of its youth and lack of a strong accretion signature. DoAr 21 is embedded in the ρ Oph star-forming region (see Wilking, Gagné, & Allen 2008 for a recent review), whereas a number of the others (e.g., TW Hya, Hen 3-600, MP Mus, V4046 Sgr with ages of $\sim$ 10–30 Myr) no longer lie in regions of active star formation, with all surrounding molecular gas having been dissipated. With an estimated age of $\lesssim$ 1 Myr (Figure 1), DoAr 21 is younger than these other stars. A few of the stars observed with high X-ray spectral resolution (e.g. T Tau, BP Tau, RU Lup) are of a similar age to DoAr 21, but all are classical T Tauri stars with strong accretion signatures. The central questions here, then, are how much difference the young age and lack of strong accretion make in the X-ray emission of DoAr 21; what the distribution and physical conditions of its circumstellar material are; and how the high-energy radiation field incident on the circumstellar material may influence its properties.

Below we discuss the stellar and circumstellar properties of DoAr 21 (Sec. 2.2), showing new images of its circumstellar material, which, surprisingly, is not present near the star but which extends to several hundred AU. We present new high-resolution optical spectra which show that DoAr 21 is not accreting but which are consistent with strong chromospheric activity. In this light, we then present our new X-ray observations (Sec. 3) and analyze the X-ray emission in detail through emission-line fits, overall fits to the thermal spectrum, and analysis of time-variability of the emission during a large flare. In Sec. 4, we discuss the interaction between the star's X-ray and ultraviolet emission and its circumstellar environment. Based on the level of activity suggested by our X-ray observations, we estimate the far-ultraviolet (FUV) flux, suggesting that it is sufficient to excite the observed PAH emission even at hundreds of AU from the star. Finally, we present a possible geometry for the H_2 emission, suggesting that it may be more akin to a photo-dissociation region (PDR) than a circumstellar disk.

2. DoAr 21's stellar properties and circumstellar environment

Before considering our new X-ray data for DoAr 21, here we consider new and existing data from other wavelengths, including new mid-infrared imaging and high-resolution optical spectroscopy. We also consider infrared and optical photometry, spectroscopy, and polarimetry from the literature in order to build up a more complete picture of the stellar properties and circumstellar environment of DoAr 21.
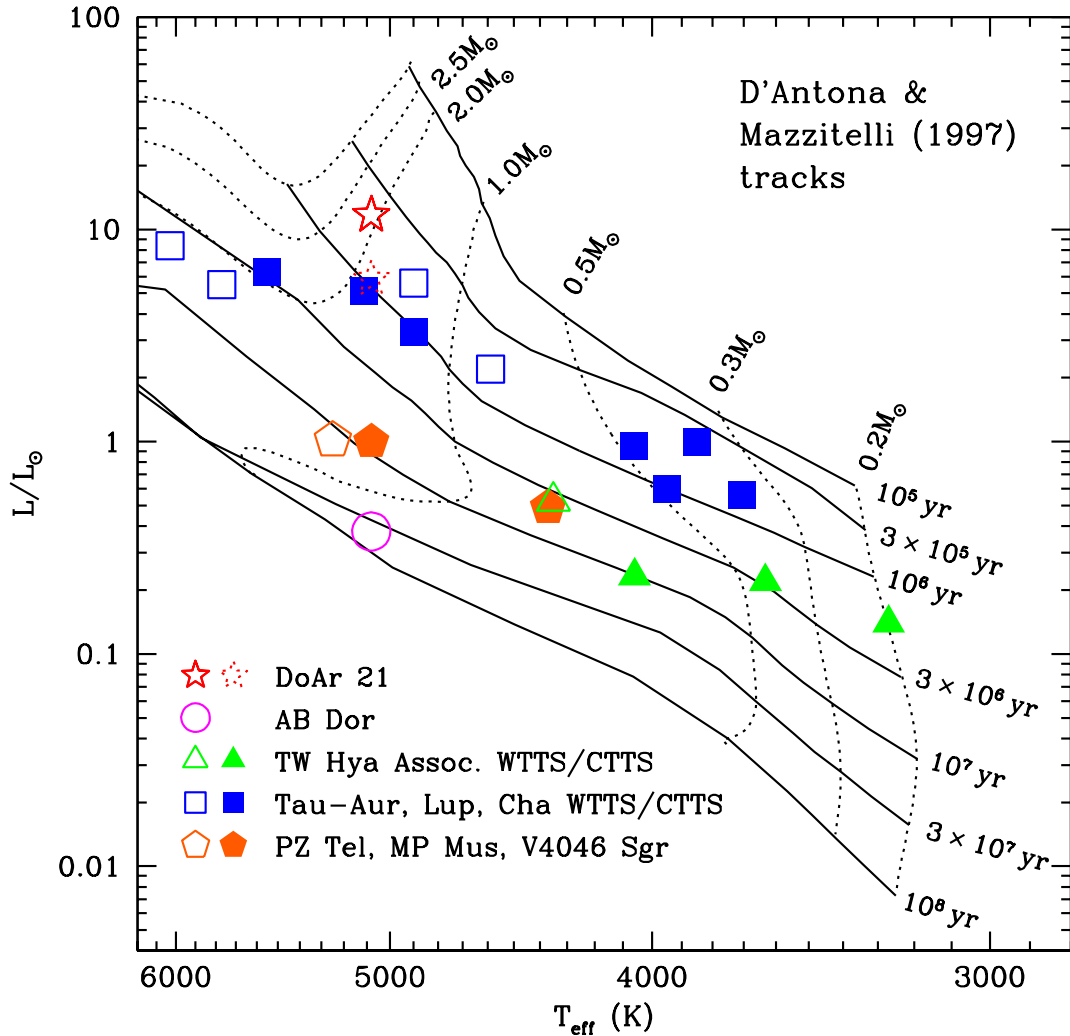
Fig. 1.— HR diagram showing the position of DoAr 21 (star symbols) compared to other pre–main-sequence stars that have been observed with the *Chandra* or XMM-Newton gratings; the dashed star shows the luminosity of each star in DoAr 21 if it is an equal-mass binary. Filled symbols are classical T Tauri stars, and open symbols are weak-lined T Tauri stars. DoAr 21 is both younger ($\sim 4 \times 10^5$ yr) and more massive (~ 2.2 M$_\odot$) than most of the T Tauri stars observed previously. The pre–main-sequence evolutionary tracks shown are from D'Antona & Mazzitelli (1997). Both the Palla & Stahler (1999) and Siess, Dufour, & Forestini (2000) tracks result in slightly older absolute ages in general, but similar relative ages.

2.1.   Stellar properties and multiplicity

Spectral types in the literature are K0 (Bouvier & Appenzeller 1992; Martín et al. 1998) from optical spectra and K0–K2 (Luhman & Rieke 1999) from near-infrared spectra. Following Luhman & Rieke (1999), we adopt a spectral type of K1 and effective temperature of 5080 K. The distance to DoAr 21 from a VLBA parallax measurement is 122 ± 6 pc (Loinard et al. 2008). Using this distance and our fit to the de-reddened spectral energy distribution (Sec. 2.2), we estimate the stellar luminosity to be 11.7 ± 0.8 $L_\odot$, where the uncertainty arises primarily from the large photometric variability and somewhat uncertain extinction.

The VLBA observations of Loinard et al. (2008) show DoAr 21 to be a binary, with a projected separation of 5 mas (0.6 AU) in one of their observations. The orbital parameters are uncertain, but Loinard et al. estimate the semimajor axis to be 1–2 AU. Since the binary pair has been detected only at radio wavelengths thus far, there is no information about the mass ratio or the optical luminosity ratio. Ascribing all of the luminosity to the primary star (filled star in Figure 1) yields a mass of ~ 2.2 $M_\odot$ and an age of $\sim 4 \times 10^5$ yr. If the luminosity is split equally between the two stars (open star in Figure 1), the mass of each star is ~ 1.8 $M_\odot$ and the age is $\sim 8 \times 10^5$ yr. There is some evidence in the optical spectra (Sec. 2.4) that the secondary is contributing to the observed line width, suggesting that its optical luminosity is non-negligible; thus the latter set of parameters may be closer to the truth. We note that DoAr 21 is relatively massive among T Tauri stars, and it has a K spectral type only because of its very young age. By an age of 3–4 Myr, it will move into the spectral type range of Herbig Ae/Be stars, and it will arrive on the main sequence as an early to mid A star.

2.2.   Spectral energy distribution and infrared excess

The evidence in the literature for circumstellar material around DoAr 21 (and accretion of such material) is mixed, and DoAr 21 has often been considered (e.g., Lada & Wilking 1984; André et al. 1992; Preibisch 1999; Bontemps et al. 2001) to be a Class III or diskless T Tauri star, though some sources have stated that it has an infrared excess (e.g., Bouvier & Appenzeller 1992), and it has recently been classified as a "transition disk" system, with a cleared inner disk but optically thick outer disk (e.g., Cieza et al. 2008).

In light of the lack of a strong infrared excess, the detection of emission features from polycyclic aromatic hydrocarbons (PAHs; Hanner, Brooke, & Tokunaga 1995) and H_2 (Bary et al. 2003; Bitner et al. 2008) was surprising, raising the possibility that a substantial

gas component of the disk is still present. Early observations showed Hα with bright and variable emission (Haro 1949), and then later weakly in emission (Dolidze & Arakelyan 1959; Hidajat 1961). Since then, however, no published observations of the star have shown Hα emission (Rydgren et al. 1976; Montmerle et al. 1983; Feigelson & Montmerle 1985; Wilking et al. 1987; Bouvier & Appenzeller 1992; Martín et al. 1998). Brγ is in absorption with no near-infrared veiling (Luhman & Rieke 1999). Our new high-resolution optical spectra (Sec. 2.4) show that the photospheric Hα absorption line is partly filled in with emission and is surrounded by weak but very broad (~ 300 km/s FWHM) emission wings, revealing a weak and variable emission component that is consistent with the Hα emission seen in older, coronally-active low-mass stars and which thus suggests that there is little to no accretion onto DoAr 21.

Despite the lack of accretion, we will show below that multiple lines of evidence point to the presence of circumstellar material around DoAr 21, but that this material is very extended and may not lie in a disk. We will argue that the unusual detection of PAH and H$_2$ emission features, and the large spatial extent of the 8–24 μm emission, is likely related to strong UV emission from DoAr 21, and perhaps partly due to its environment in the ρ Oph cloud.

The spectral energy distribution (SED) of DoAr 21 gives some clues to the nature of its circumstellar environment. We searched the literature for available photometry of DoAr 21, and assembled the SED from $\lambda = 0.39$ μm (U band) to $\lambda = 1.3$ mm. The observed broad-band colors are much redder than photospheric colors for a K1 star. To de-redden the photometry and to determine whether or not DoAr 21 shows any evidence of infrared excess, a signature of the presence of a circumstellar disk, we compared the SED of DoAr 21 to a model photosphere (Buser & Kurucz 1992) with $T_{\rm eff} = 5000$ K (Figure 2). We adopt the extinction law of Weingartner & Draine (2001a), with the modifications of Draine (2003). This extinction law has been shown to be a better fit to mid-infrared data than a power-law extrapolation from the near-infrared (Román-Zúñiga et al. 2007; Chapman et al. 2008; McClure 2008). We use a ratio of total-to-selective extinction $R_V \equiv A_V/E(B-V) = 4.2$, determined from the relationship $R_V = 5.7\lambda_{\rm max}$ (Vrba et al. 1993), where $\lambda_{\rm max} = 0.74$ μm is the wavelength of maximum observed polarization for DoAr 21 (Martin et al. 1992). This value of R_V is consistent with results found for other lines of sight in Ophiuchus (Vrba et al. 1993) and yields a notably better fit to the $UBVRI$ data than the standard interstellar value of $R_V = 3.1$. Physically, a larger R_V corresponds to larger grain sizes, as expected in a dense cloud. Using this extinction law, we de-reddened the photometry to find the best fit of the model photosphere to the V, R, and I data, as the U and B data show significant variability and the longer-wavelength data may be affected by any infrared excess. This procedure yielded $A_V = 6.2$ mag, and combined with our adopted distance, a photospheric

luminosity of $11.7 \pm 0.8 \, L_{\odot}$. This extinction corresponds to $A_J = 1.8$. We note that this is consistent with the neutral hydrogen column density of $N_H \approx 10^{22}$ atoms cm^{-2} found from the X-ray spectrum (Sec. 3); from a sample of 20 sources with good X-ray and infrared data in the ρ Oph cloud, Vuong et al. (2003) find $N_H/A_J = 5.6 \pm 0.4 \times 10^{21}$ cm^{-2} mag^{-1}. Given the differences in extinction laws used, our adopted extinction is reasonably consistent with that found by other authors; Luhman & Rieke (1999) find $A_J = 1.6$ mag, and Bouvier & Appenzeller (1992) find $A_V = 6.6$. The de-reddened photometric data are plotted in Figure 2; the millimeter-wavelength upper limits of André et al. (1990) and Cieza et al. (2008) are not shown.

While the observed optical and near-infrared variability (see Section 4.1.5) makes it impossible to fit every data point, the photometry is broadly consistent with the model photosphere within the uncertainties for $\lambda \leq 5 \, \mu$m. There is some evidence for excess emission at U and B, which may be due to flaring as discussed below. While the brightest U and B points are clearly inconsistent with photospheric emission, the fainter points lie close to the model photosphere, consistent with a scenario in which DoAr 21 is flaring much of the time.

At longer wavelengths, there is a clear infrared excess at $\lambda = 7$–$24 \, \mu$m. These points are quite insensitive to extinction corrections, since the extinction is so small, and to the determination of the star's effective temperature, since they lie on the Rayleigh-Jeans tail of the photospheric emission. The space-based infrared data are highlighted in the figure as squares (orange in the on-line edition), as they are not affected by the Earth's atmosphere and are measured on a uniform photometric system; the $\lambda = 6.7$ and $14 \, \mu$m points are ISO data from Bontemps et al. (2001), while the other $\lambda = 3.6$–$24 \, \mu$m squares are *Spitzer* IRAC and MIPS data from Cieza et al. (2007). While the presence of an excess shortward of $7 \, \mu$m is debatable, the 8–$24 \, \mu$m points are well in excess of the photospheric emission, indicating the presence of some circumstellar disk material within a radius of $4''$–$9''$, the aperture size of the mid-infrared observations. This circumstellar material apparently does not have a large mass in small dust grains, however, given the very sensitive 3σ flux upper limits of < 4 mJy at $\lambda = 1300 \, \mu$m (André et al. 1990) and < 18 mJy at $\lambda = 850 \, \mu$m (Cieza et al. 2008).

2.3. Mid-infrared imaging

2.3.1. Archival Spitzer images

DoAr 21 was observed by the *Spitzer* Space Telescope with both IRAC ($\lambda = 3.6$, 4.5, 5.8, 8.0 μm) and MIPS ($\lambda = 24$, 70, and 160 μm) as part of the c2d Legacy program (Cieza
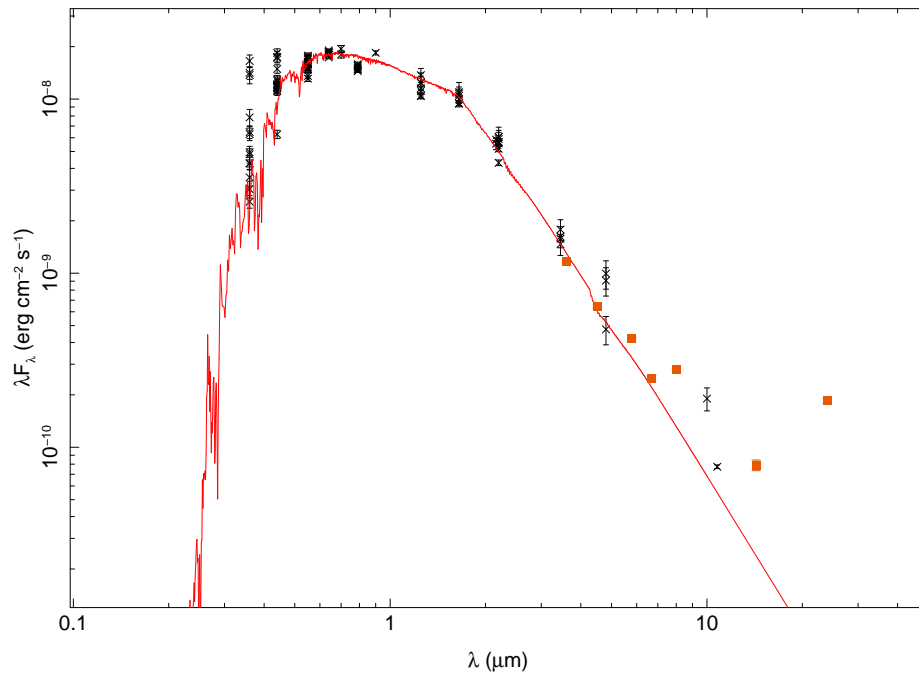
Fig. 2.— The spectral energy distribution of DoAr 21, from ultraviolet through infrared wavelengths. Spitzer and ISO data are shown as filled squares (orange in the on-line edition), and the 850 μm and 1.3 mm upper limits are not shown. The photometry has been de-reddened with $A_V = 6.2$ and $R_V = 4.2$ as described in the text. Overplotted is a model photosphere (solid line); the star shows a clear infrared excess at $\lambda \geq 8$ μm.

et al. 2007; Padgett et al. 2008). PSF-fitting photometry of DoAr 21 from 3.6–24 μm is reported by Cieza et al. (2007) and plotted in Figure 2; here we concentrate on the images themselves. Figure 3 shows the $\lambda = 24$ μm image of the region around DoAr 21; DoAr 21 itself is clearly detected. Visual examination of the $\lambda = 70$ μm images shows a source at the position of DoAr 21, but the noise is too high for accurate photometry.

Surprisingly, the 24-μm emission from DoAr 21 is somewhat extended. Close inspection of the 24-μm MIPS images reveals that the profile of DoAr 21 is different from that of other stars in the field. Since *Spitzer* is diffraction-limited at 24 μm, the point-spread-function (PSF) is a modified Airy pattern, and indeed many of the sources in Figure 3 (including sources that are fainter than DoAr 21 and/or projected on comparable or brighter background emission) show the presence of the first Airy ring. DoAr 21 does not, however, indicating that it is not a point source at 24 μm. To check this, we compared the azimuthally-averaged radial profile of DoAr 21 to that of a star in the same image (GSS 26), and also to a sample empirical on-orbit PSF (constructed from many stars in a MIPS mosaic image of the Trapezium) supplied by the Spitzer Science Center (SSC). DoAr 21 is clearly more extended than the other stars, both of which show the signature of the first Airy ring at radii of 3–5 pixels, while DoAr 21 does not. (The diffraction limit of *Spitzer* at 24 μm is $7\rlap{.}''4$, while the MIPS mosaic pixel size is $2\rlap{.}''45$, so the first null occurs at a radius of 3 pixels.) We examined three different MIPS mosaic images, and DoAr 21 appears extended in all of them. We also examined the individual baseline-calibrated data (BCD) frames from the SSC archive (from which the mosaics were constructed), and found that DoAr 21 appears extended in each frame, regardless of its position on the chip, while other stars in the frame do not. Thus, the broader profile of DoAr 21 is not an artifact of the mosaicing process.

To estimate the radial extent of the emission, we convolved an oversampled MIPS PSF with Gaussians of different radii, resampled them at the MIPS pixel scale, and compared their radial profiles to that of DoAr 21. The profile of DoAr 21 is roughly consistent with a Gaussian source with a sigma of 0.75–1 MIPS pixel ($1\rlap{.}''8$–$2\rlap{.}''5$). At the 122 pc distance of DoAr 21, this corresponds to a FWHM of 500–700 AU. Thus, the 24-μm emission appears to be extended to radii of 250–350 AU from the star.

2.3.2. New Gemini images

Motivated by the extended emission seen in the *Spitzer* images, we observed DoAr 21 with the T-ReCS camera on Gemini South in June and July 2007. The observations were made through filters with central wavelengths (and 50% transmission widths) in μm of 8.6 ($\Delta\lambda = 0.43$), 10.4 ($\Delta\lambda = 1.02$), 11.3 ($\Delta\lambda = 0.61$), and 18.3 ($\Delta\lambda = 1.51$). The 8.6 and
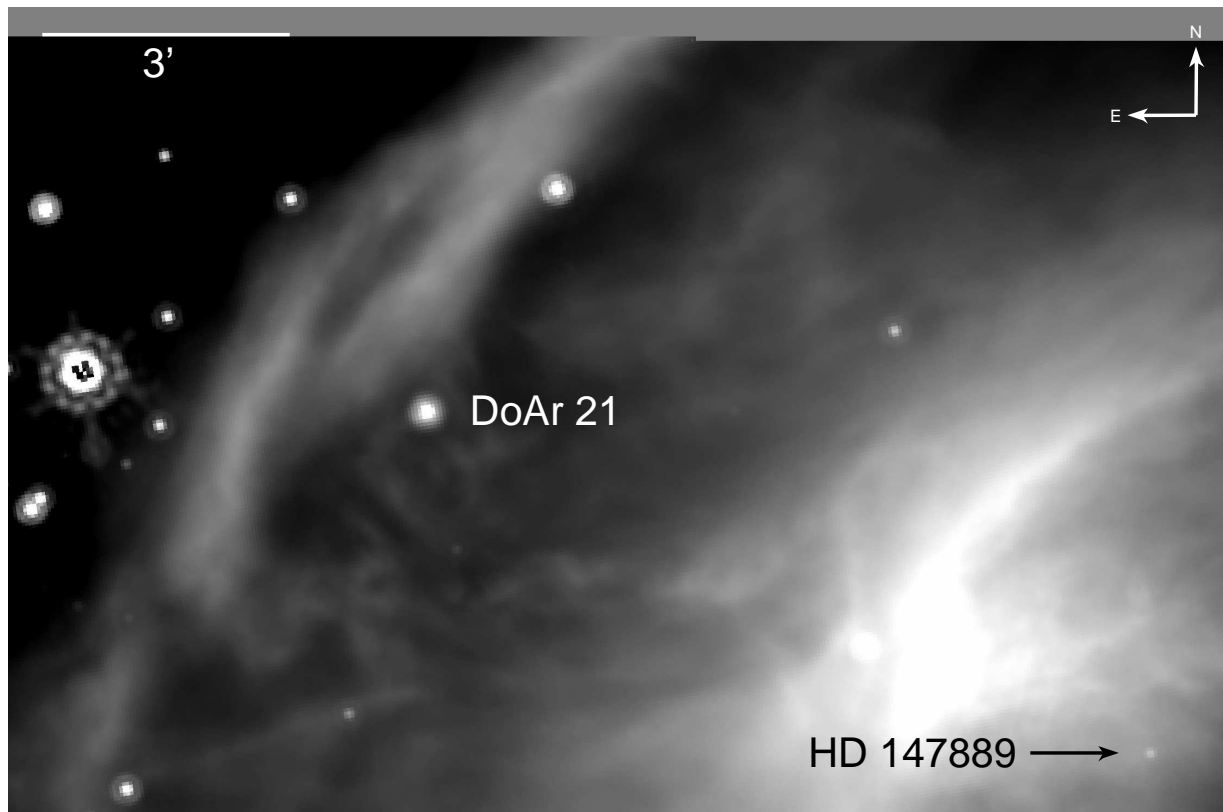
Fig. 3.— *Spitzer* MIPS 24-μm image of the field around DoAr 21; DoAr 21 is clearly detected, indicating a substantial amount of circumstellar material. Unlike other stellar sources in the field, DoAr 21 does not show the first Airy ring, indicating that the 24-μm emission is marginally resolved.

11.3 μm filters are centered on PAH features, while the 10.4 μm Si-4 and 18.3 μm Qa filters largely measure continuum emission. In particular, the Si-4 filter acts as a nearby continuum reference for any PAH emission.

The data were taken with the standard chop and nod technique to remove sky background emission, and were processed with the standard Gemini IRAF pipeline. The chop throw was $15''$ at a position angle of $130°$, parallel to the ridge of 24-μm emission seen in the *Spitzer* images (Figure 3); this chop direction was chosen to minimize variation of the background emission.

The data were flux-calibrated with observations of HD 136422 (K5 III) at a similar airmass and near in time to the DoAr 21 observations in each filter. Fluxes for HD 136422 were taken from the calibrated template spectrum created by Cohen et al. (1999). Because the target and calibrator were observed at similar, low ($\lesssim 1.3$) airmasses and near in time to each other, we did not attempt to correct for differential atmospheric extinction between target and calibrator observations.

The spatial resolution of our observations, as measured by the FWHM of standard stars observed at similar airmass to DoAr 21, was $0\rlap{.}''35$–$0\rlap{.}''38$ in the 8.6–11.3 μm observations, and $0\rlap{.}''58$ at 18.3 μm. This is near the diffraction limit of Gemini South, and is well-sampled by the T-ReCS pixel scale of $0.09''$ pixel^{-1}.

The resulting images are shown in Figure 4. Irregular, extended emission is seen at all wavelengths. The emission is brighter and more extended in the filters containing PAH features (8.6 and 11.3 μm) than in the 10.4 μm continuum, suggesting that the extended material shows PAH emission. The brightest off-source emission is a spot roughly $1\rlap{.}''1$ north of DoAr 21, and there is a ridge or partial arc of emission to the north and west, seen in all filters except 10.4 μm.

The central stellar source in the 8.6–11.3 μm DoAr 21 images appears point-like at our resolution; it has a FWHM similar to that of the photometric calibrator in the corresponding band. The slight extension of the PSF at PA $\sim 230°$ in the 8.6 μm images is also seen in the calibrator. The central source in the 18.3 μm image has FWHM of $0\rlap{.}''6$–$1\rlap{.}''0$; given the much lower signal-to-noise ratio at this wavelength, it is difficult to tell if the central source is extended, though certainly there is significant extended emission beyond this.

The extended emission is quite asymmetric, unlike the emission expected from a disk. There is a partial arc or ring to the north and west (seen most prominently at 11.3 and 18.3 μm) at roughly $1\rlap{.}''1$ from the star. There are bright knots at position angles of roughly $0°$ and $140°$, with the northern knot appearing both brighter and more concentrated, and the SE knot being visible to larger radii, especially at 18.3 μm. As shown in the star-subtracted
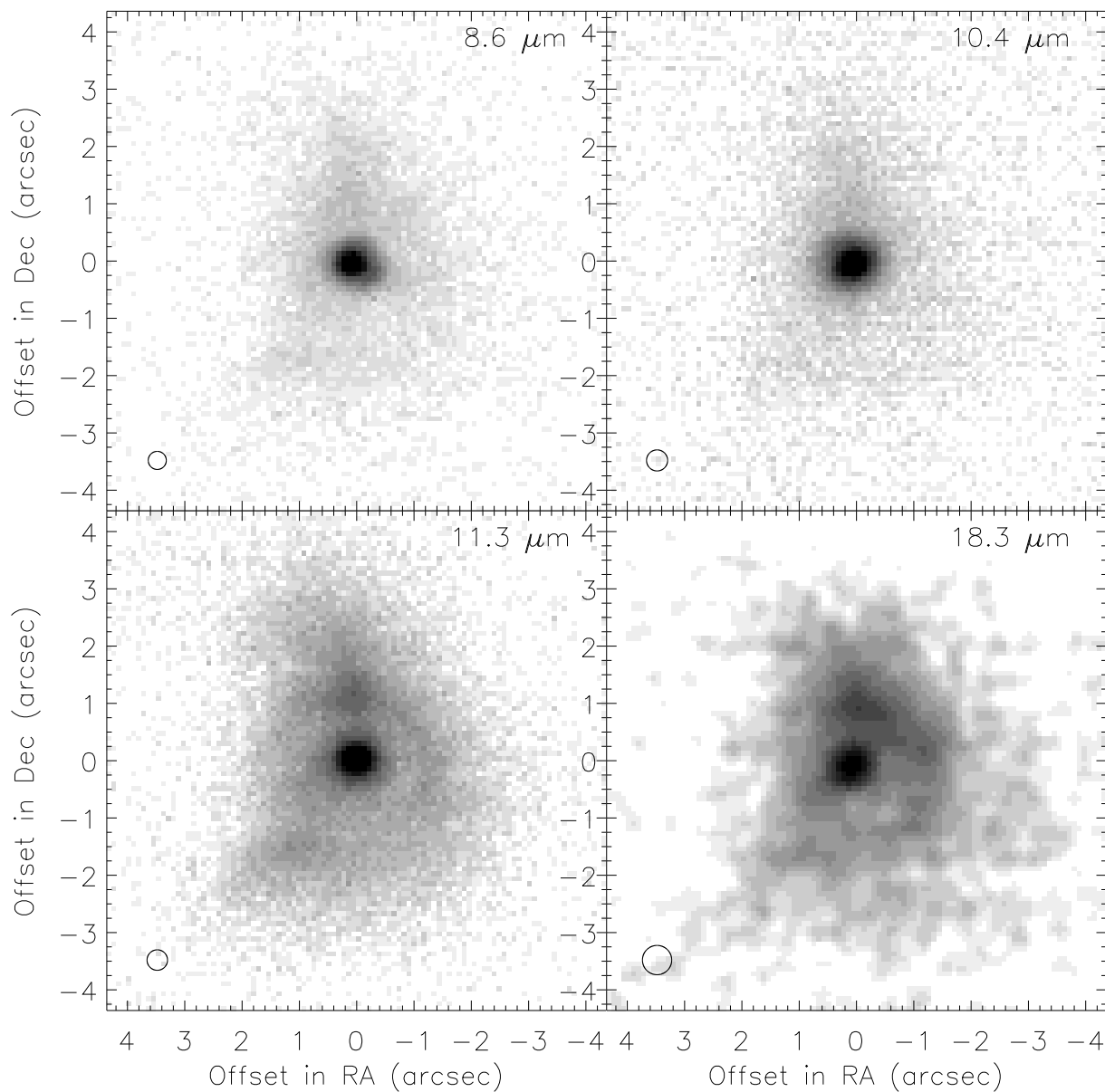
Fig. 4.— Gemini T-ReCS images of DoAr 21 at four different wavelengths. The grayscale shows the emission displayed with a logarithmic stretch; the 18.3-μm image is smoothed with a 3-pixel FWHM Gaussian. The circle in the lower left of each image shows the FWHM of the PSF measured from a comparison star observed at similar airmass.

azimuthal profile in Figure 5, there is a roughly 4:1 contrast between the brightest and faintest position angles.

Archival HST WFPC/2 images of DoAr 21 in the F606W and F814W filters show a faint filament extending southeast from the star; the filament is not apparent in images in the F1042M filter. There is no obvious brightness gradient along the filament, so Stapelfeldt et al. (2009) suggest that it is foreground or background material illuminated by the star, rather than a jet reaching near the stellar surface. This filament is also visible in the narrow-band near-infrared images of Gómez et al. (2003), in filters both on and off the H_2 1–0 S(1) line. Comparison of the WFPC/2, near-IR, and Gemini images shows that this filament overlaps the extension seen in Figure 4 at PA 140°. Thus, the circumstellar material apparently extends to even larger radii than seen in our images, at least in some directions. We discuss this point further in Section 4.

To quantify the spatial distribution of circumstellar material, and in particular to see whether there is any infrared excess emission that is not spatially resolved, we measured the flux in our images in apertures of different radii. We chose aperture radii of 0''82, 2''75, and 6''. The smallest radius corresponds to a physical radius of 100 AU, a typical disk radius for a young star; the intermediate radius matches the aperture used by Hanner, Brooke, & Tokunaga (1995) for their mid-infrared spectroscopy; and the largest radius encompasses all the detected flux above the background level in our images, probing roughly the same spatial scale as the MIPS 24-μm images. These fluxes are quoted in Table 1 and plotted in Figure 6. There is little infrared excess within 100 AU of the star, while the photometry of the more extended emission is roughly consistent with previous photometry.

Given the clear presence of a significant amount of circumstellar material, but evidence that little of it is close to the star, we now turn to the question of whether there is any evidence for accretion onto DoAr 21.

Table 1.   Photometry of DoAr 21

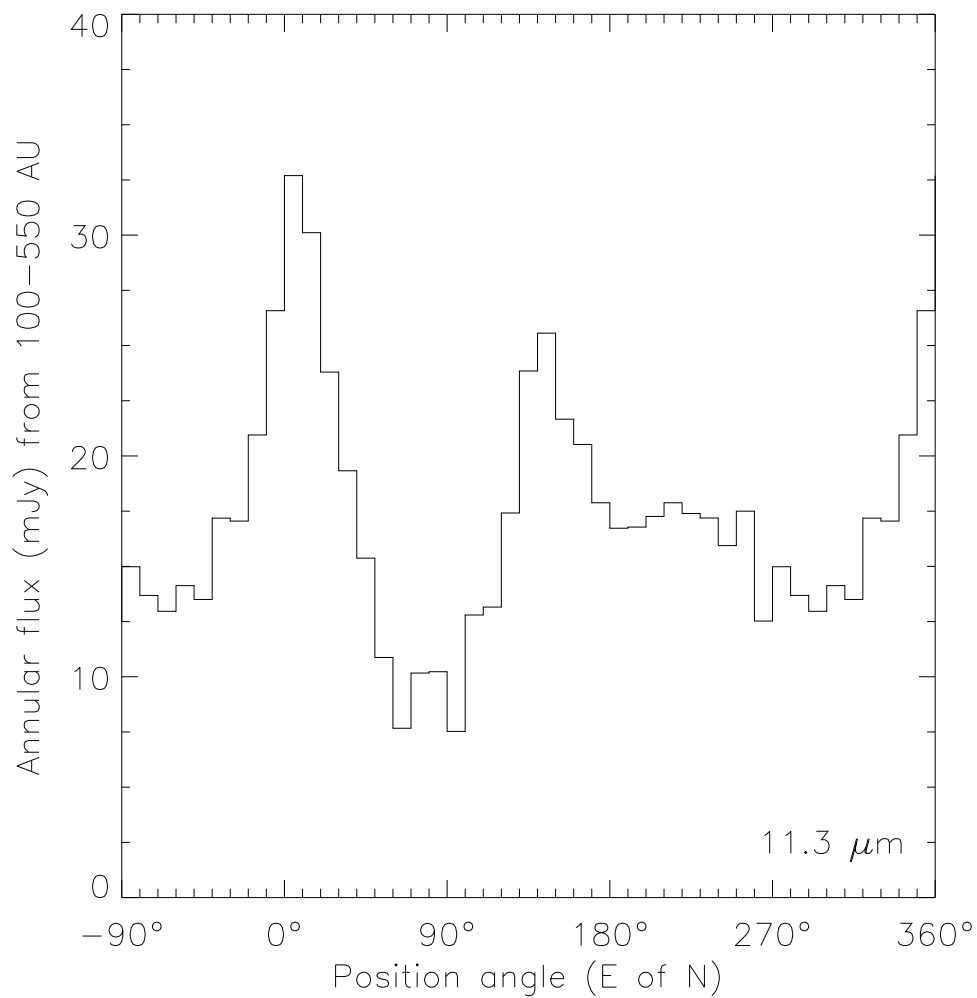| Filter	Flux within 0''82 (mJy)	Flux within 2''75 (mJy)	Flux within 6'' (mJy)
8.6 μm (PAH)	313	525	596
10.4 μm (Si-4)	176	300	347
11.3 μm (PAH)	234	680	816
18.3 μm (Qa)	165	607	728

Fig. 5.— Azimuthal profile of the 11.3-μm emission between radii of 100 AU and 550 AU, showing the 4:1 contrast in brightness at different position angles. The profiles in the 8.6 μm and 10.4 μm images show similar structure and contrast, though at lower flux levels.
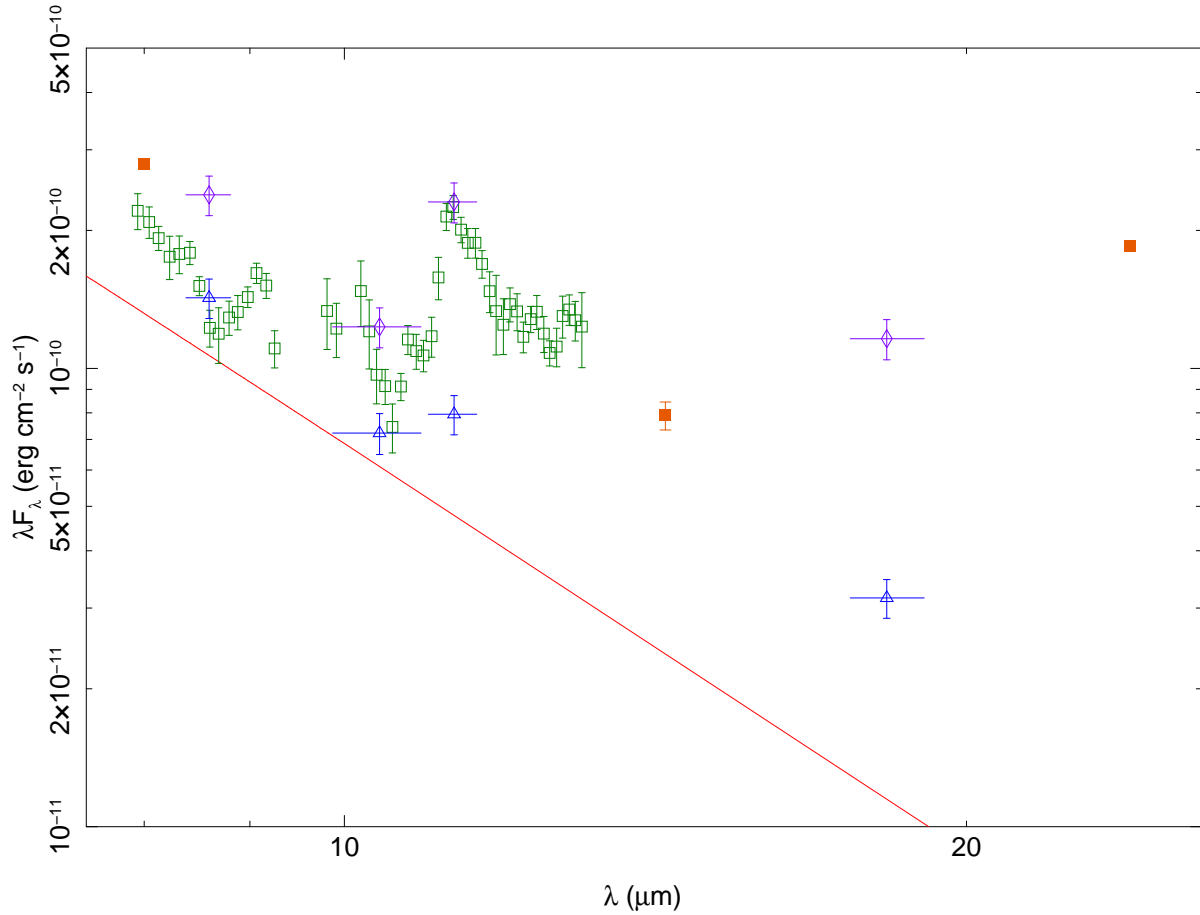
Fig. 6.— A close-up of the mid-infrared SED, with the model photosphere and de-reddened photometry as in Figure reffigure:sed. The broad-band Spitzer and ISO data are show as filled squares (orange in the on-line edition), and the spectrum from Hanner, Brooke, & Tokunaga (1995) is shown as open squares (green in the on-line edition), showing an emission feature at 11.3 μm attributed to polycyclic aromatic hydrocarbons (PAHs). De-reddened photometric measurements from new Gemini narrow-band images are overplotted, with horizontal bars showing the bandwidth of the filters used and vertical error bars showing the assumed 10% uncertainty. The open triangles (blue in the on-line edition) show measurements within 100 AU of the star, showing little or no excess in the continuum at 10.4 μm. The open diamonds (purple in the on-line edition) show measurements in a 5''5 diameter aperture, the same as that used by Hanner, Brooke, & Tokunaga (1995).

2.4.   Optical spectrum

As noted in Section 2.2, the Hα emission from DoAr 21 has shown varying behavior at different times in the past, and thus additional spectroscopic observations are useful to probe this behavior. In addition, DoAr 21's stellar rotation period is unknown, as it did not show periodic photometric variability in the observations of Bouvier et al. (1988).

To probe the Hα emission and stellar rotation of DoAr 21, we observed it with the echelle spectrograph on the CTIO Blanco 4-meter telescope on 2002 June 12 and 14, and on the four consecutive nights 2003 April 11–14. The spectrograph setup gave wavelength coverage of approximately 5,000–8,000 Å with 0.08 Å/pixel. With a 1$''$ slit width, this gave a spectral resolution (as measured from the FWHM of narrow lines in a ThAr comparison lamp spectrum) of $R = 40,000$ at the Hα line. Exposure times were 20 minutes on 2002 June 12, 15 minutes on 2003 April 11 and 30 minutes on the other four nights. The data were reduced using standard routines for echelle spectra in IRAF.[2]

Comparison of these spectra with a K1 V standard spectrum artificially broadened to various velocities gives a projected rotational velocity $v \sin i = 80 \pm 10$ km s^{-1} for DoAr 21. Combined with the stellar radius of 4.6 R$_\odot$ estimated from its effective temperature and luminosity (attributing all the luminosity to one star), this gives a rotational period of around 3 days, or less if the star is not viewed equator-on.[3]

Given the discovery that DoAr 21 is a binary (Sec. 2.1), however, there is an alternate interpretation of the width of its spectral lines. Massarotti et al. (2005) report $v \sin i = 29$ km s^{-1} for DoAr 21. The origin of the discrepancy between their determination and ours is unclear, but it could result from observing a binary at different orbital phases, so that sometimes the lines are broadened (though not clearly doubled) due to different radial velocities of the two stars. The Massarotti et al. (2005) spectra, measured at similar spectral resolution but with less spectral coverage and lower S/N, show some variation in the width of the cross-correlation peak, which is a measure of the line width, occasionally showing broader peaks (D. Latham, personal communication). Our spectra show consistently broad lines, and none of our six spectra is consistent with $v \sin i$ as low as 29 km s^{-1}. We repeated the procedure used by Massarotti et al. (2005) on our spectra, cross-correlating various

---

[2]IRAF is distributed by the National Optical Astronomy Observatories, which are operated by the Association of Universities for Research in Astronomy, Inc., under cooperative agreement with the National Science Foundation.

[3]Bary et al. (2003) suggest that the inclination DoAr 21 is greater than 55°. If this is the case, then the equatorial rotational velocity is greater than 100 km s^{-1}.

artificially broadened template spectra with DoAr 21 to find the template that gives the highest correlation peak, and we consistently find $v \sin i \approx 80$ km s^{-1}. However, our spectra cover only two windows of a few days each, so it is possible that both our 2002 and 2003 observations were obtained at orbital phases with relatively large velocity differences. If we assume an equal-mass binary, the evolutionary tracks in Figure 1 give masses of ~ 1.8 $M_\odot$ for each star, or a total system mass of ~ 3.6 $M_\odot$. With an assumed semimajor axis of 1–2 AU (Loinard et al. 2008), the relative orbital velocity of the two stars in a circular orbit would be $\sim$40–60 km s^{-1}, which is of the right magnitude to account for the difference in line broadening observed in our spectra and those of Massarotti et al. (2005). The inferred orbital period of 0.5–1.5 yr from these orbital parameters is also consistent with our two observations (separated by ten months) falling either half or a whole orbital period apart, so that the same velocity difference would be observed.

DoAr 21 has at times shown Hα in emission in the past (Haro 1949; Dolidze & Arakelyan 1959), while other observations have shown Hα absorption. Our observations, shown in Figure 7, show a combination of both. There is a central photospheric absorption line, but our high spectral resolution reveals the presence of broad emission wings. In addition, comparison with the K1 V spectral standard HD 13445 (Keenan & McNeil 1989), artificially broadened to $v \sin i = 80$ km s^{-1}, shows that DoAr 21's Hα absorption line is substantially filled in with emission.

Further, the line varies substantially from one night to the next. Figure 7b shows the difference between two nights, clearly showing the presence of a broad, variable emission component at Hα. The emission shown here is a lower limit to the true Hα emission line flux, since any emission component present on both nights is subtracted out. The FWHM of the emission is $\sim$ 300 km s^{-1}, while the full width at 10% intensity is $\sim$ 450 km s^{-1}. White & Basri (2003) propose that stars with Hα full width at 10% intensity of > 270 km s^{-1} should be considered classical T Tauri stars, arguing that the line velocity width is a better accretion diagnostic than the more commonly used equivalent width. By this measure, DoAr 21 could be considered to be a classical (accreting) T Tauri star, and indeed Bary et al. (2002) suggest that DoAr 21 is still accreting material from a disk based on their detection of H$_2$.

However, some stars that are not thought to be accreting show Hα behavior similar to that seen in DoAr 21. Montes et al. (1997) find that some chromospherically active binary stars show Hα emission that is well-fit by a broad component and a narrow component, with the broad component having FWHM values from 133 to 470 km s^{-1}. Fernández et al. (2004) find that the quiescent (non-flare) spectrum of the weak-lined pre–main-sequence triple system V410 Tau has Hα that is just filled in, not overtly in emission, while during
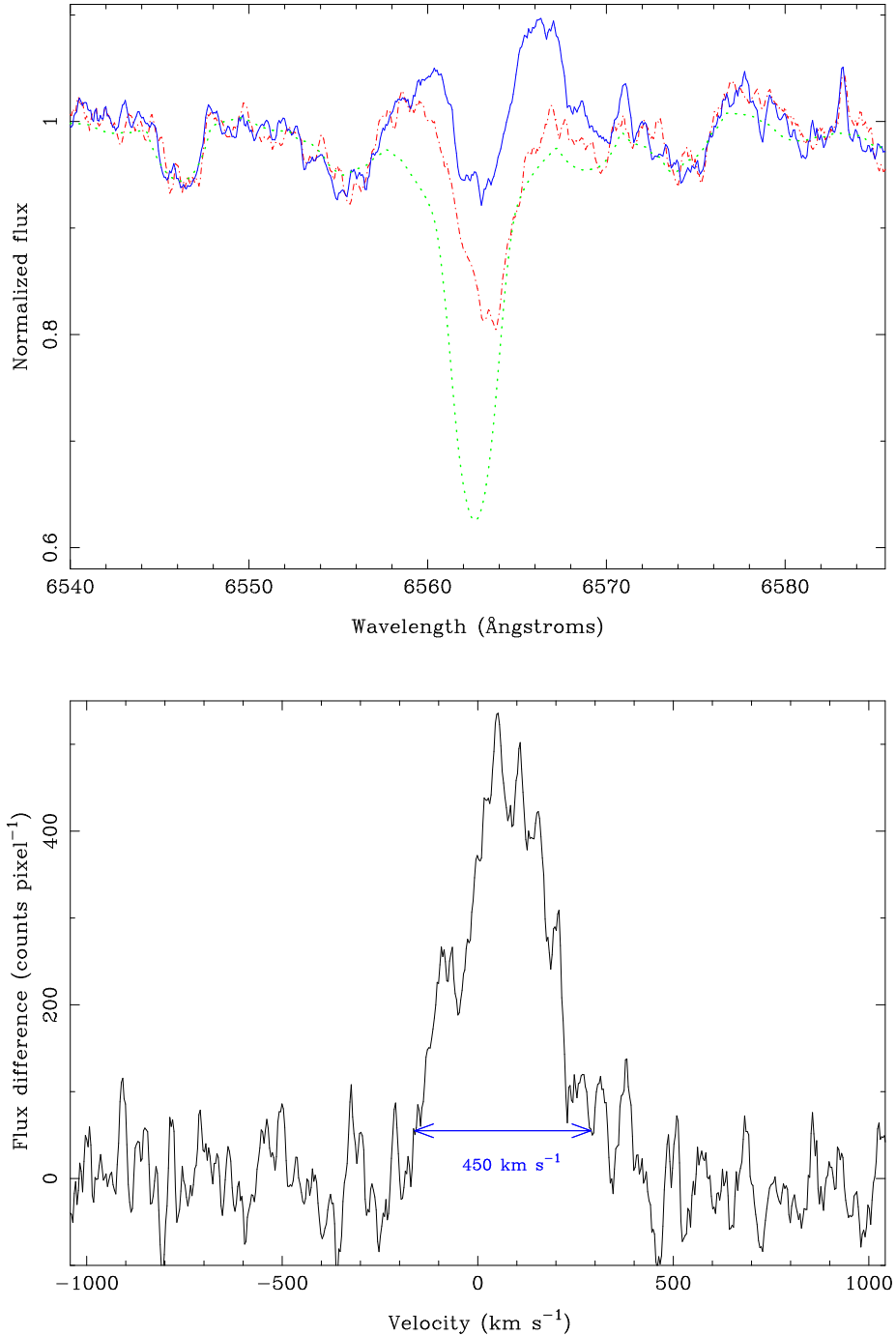
Fig. 7.— High-resolution optical spectra of DoAr 21 in the vicinity of the Hα line. Top: The dot-dashed line (red in the online edition) shows DoAr 21 on 12 April 2003; the solid line (blue in the online edition) shows DoAr 21 on 13 April 2003; the dotted line (green in the online edition) shows the K1 V standard star HD 13445, artificially broadened to $v \sin i = 80$ km s^{-1}. The Hα line in DoAr 21 clearly is filled in by a broad emission component that is present on both nights, but stronger on the second night. Bottom: The difference between the two DoAr 21 spectra, showing the broad emission component that appears the second night. The full-width at 10% intensity is indicated.

a flare the Hα equivalent width is 27 Å. After subtraction of a photosphere of the correct spectral type from the quiescent spectrum, they find that the residual Hα emission line (equivalent width $\sim$ 1 Å, similar to the emission component from DoAr 21) has a broad component with a FWHM of 300–400 km s^{-1}. During a flare, the Hβ line is observed to be in emission with FWHM of 730 km s^{-1}, with its width declining as the flare decays. V410 Tau shows no evidence of infrared excess or other indicators of accretion, though definitive detection of a very weak infrared excess might be difficult given the shortage of resolved infrared measurements of the three stars (all within 0$\farcs$3; White & Ghez 2001) in the system. There is no detectable emission in the CO fundamental (Najita, Carr, & Mathieu 2003) nor H$_2$ FUV lines (Herczeg et al. 2006). With no evidence of either a gas or a dust disk, the Hα seems more likely to be related to the flares than to accretion. Thus, broad Balmer emission lines are not by themselves an unambiguous indicator of accretion.

We revisit the question of what the Hα and H$_2$ emission tell us about DoAr 21's circumstellar material in Section 4. Here we simply note that the chromospheric activity implied by one interpretation of the Hα emission and the need for a strong UV flux to excite the H$_2$ and PAH emission both imply a need for a better understanding of the high-energy emission from DoAr 21. Thus, we now turn to an examination of our new high-resolution X-ray spectrum of DoAr 21.

3. X-ray emission

DoAr 21 is the brightest X-ray source in the ρ Oph cloud core A, with an X-ray luminosity of nearly 10^{32} ergs s^{-1}, a hard thermal spectrum, and large X-ray flares seen in several archival observations at a rate of nearly one per day. Its X-ray emission has been observed at low resolution with *Einstein* (Montmerle et al. 1983), *ROSAT* (Casanova et al. 1995), *ASCA* (Koyama et al. 1994), and *Chandra* (Imanashi et al. 2002; Gagné et al. 2004).

The new *Chandra* grating spectra we present here have vastly superior spectral resolution compared to any of these previous datasets, enabling us to extract temperature and abundance information with more reliability and also, for the first time, to examine density diagnostics. Given the high rate of flaring seen in previous observations, it is not surprising that we detected a large and time-resolved flare in our 94 ksec *Chandra* observation. We can bring some of these same diagnostic tools to bear on the pre-flare, flare, and post-flare portions of the new dataset.

The High Energy Transmission Grating Spectrometer (HETGS) has two grating arrays: the Medium Energy Grating (MEG), with a FWHM resolution of 2.3 mÅ; and the High

Energy Grating (HEG), with a resolution of 1.2 mÅ (Canizares et al. 2005). Both grating arrays operate together, with the dispersed spectra (first, second, and third orders) as well as the zeroth order spectrum recorded on the ACIS CCD array. We used standard CIAO (v.3.3) tools to extract the dispersed spectra, and to create observation specific spectral response matrices and effective area tabulations, as well as to create light curves and also to extract spectra for each of the three subsets of the observation. Of the dispersed spectra, only the first order spectra have a significant number of counts. The zeroth order spectrum is severely piled up, so we restrict the analysis we report on here to the first order MEG and HEG spectra. We performed most of the spectral analysis using XSPEC v.12.3.

The goal of our X-ray spectral and timing analysis is to characterize the properties of the hot plasma on this very magnetically active pre-main-sequence star, and to compare its properties to those measured in other PMS stars with high-resolution X-ray spectra. Its extreme youth and lack of obvious signatures of accretion make for an interesting contrast between DoAr 21 and the strongly accreting T Tauri stars that have been well-studied with the *Chandra* gratings (Güdel & Telleschi 2007). Although DoAr 21 is not a classical T Tauri star, it does—as we have detailed in the previous section—have some circumstellar material in its vicinity. The observed X-rays, and the unobservable far- and extreme-UV emission associated with the X-ray emitting plasma as it cools, could have an important effect on this circumstellar material, perhaps being the dominant source of excitation for the PAH emission. Thus, characterizing the X-ray properties of the star is important for understanding the physical conditions in the circumstellar environment.

In Fig. 8 we show the MEG and HEG spectra (negative and positive first orders co-added in both cases), with emission lines identified and labeled. Although the *Chandra* gratings and detector have significant response to wavelengths above 30 Å, interstellar attenuation (due to photoelectric absorption, which has a cross section that goes roughly as λ^3) makes the spectra above 12 Å nearly devoid of counts. These spectra are dominated by a strong bremsstrahlung continuum, which is indicative of plasma with a dominant temperature well in excess of 20 million K (so that atoms are mostly fully stripped and their associated line emission is weak). The presence of emission from high ion stages – up to helium-like Fe XXV and hydrogen-like Fe XXVI – also indicates very high plasma temperatures. We analyze the temperature distribution in the plasma in detail below by fitting thermal emission models to the entire spectrum.

Fig. 8.— The entire usable portions of the MEG (top) and HEG (bottom) co-added (negative and positive) first order spectra of DoAr 21. The bin sizes are 2.5 mÅ for the HEG and 5 mÅ for the MEG. The shape of the continuum is dominated by the wavelength-dependent effective area of the telescope, gratings, and detector, rather than the intrinsic emission. Vertical dashed lines represent the laboratory rest wavelengths of all detected emission lines. The annotations above the top panel indicate the element and ionization stage of each line, while those above the lower panel highlight the Lyman-α lines of the hydrogen-like isoelectronic sequence and the principal transition of the helium-like isoelectronic sequence.

3.1. Spectral Modeling

We fit the MEG and HEG first order dispersed spectra simultaneously (but not co-added) over the spectral ranges where each has a significant number of counts. For the MEG this was 2–12.5 Å, and for the HEG it was 1.5–11.5 Å. We fit a two-temperature optically thin thermal emission model (the *bapec* implementation of the Astrophysical Plasma Emission Code (APEC) (Smith et al. 2001)) that accounts for bremsstrahlung and line emission from a plasma in statistical equilibrium. This model has four free parameters: the plasma temperature, the abundances (expressed as a fraction of solar), the emission measure ($4\pi d^2 \int n_e n_H dV$, proportional to the normalization of the model), and the line broadening, which is an ad hoc turbulent velocity added in quadrature to the thermal velocity of each line in the model. We also include interstellar attenuation, with cross sections from Morrison & McCammon (1983). We used the χ^2 statistic with Churazov weighting to assess goodness of fit and to place confidence limits on the derived model parameters.

A single temperature model does not provide a good fit, though the low resolution *ASCA* and *Chandra* ACIS data are adequately fit by a single temperature thermal model (Imanashi et al. 2002). We did find a good fit when we used a two temperature *bapec* model with interstellar absorption. The best-fit model has temperatures of roughly 12 and 48 million K (MK), with approximately five times the emission measure in the hotter component as in the cooler component. The abundances are sub-solar, and no significant line broadening is found, with a 68 percent confidence limit of $\sigma_{turb} = 50$ km s^{-1}; about one-third of the peak spectral resolution. We find an interstellar column density of slightly more than 10^{22} cm^{-2}, which is completely consistent with the extinction of $A_V = 6.2$ magnitudes, given the conversion between extinction and hydrogen column density of Vuong et al. (2003). The model has a flux of 1.48×10^{-11} ergs s^{-1} cm^{-2} on the range 0.3–10 keV. Correcting for interstellar attenuation, the unabsorbed X-ray flux is a little more than twice this, corresponding to an X-ray luminosity of $L_X = 5.44 \times 10^{31}$ ergs s^{-1}. The best-fit model parameters and their 68 percent confidence limits are listed in the first row of Table 2. This fit is formally good, although the two temperatures certainly are an approximation to a continuous distribution of temperatures. Furthermore, the confidence limits are based only on statistical errors on the data, and in our experience, for datasets with many bins (the data we fit here have 12,196 bins), formal confidence limits are unrealistically tight.

To test the robustness of this fit, we refit the data using the ISIS X-ray analysis package (ver. 1.4.9-38) (Houck & Denicola 2000). We used the APEC model with interstellar absorption, and – as we did with the fits in XSPEC – found that a two temperature model was required to achieve a good fit. The temperatures of the best-fit components were both higher by about 20 percent, and the emission measure weighting was even more skewed toward the

hot component in this ISIS fit compared to the XSPEC fit. The interstellar column density was about 10 percent lower than in the XSPEC fit. There were some differences in the method used for the fitting in ISIS, including the use of the C statistic (Cash 1979) and a somewhat different wavelength range (1.8–18 Å for both the MEG and HEG data). Perhaps these 10–20 percent discrepancies between the results from the two model fitting programs are a more realistic representation of the parameter uncertainties than are the formal, statistical confidence limits. We will use the APEC model fitting in XSPEC as the standard throughout the rest of the paper.

The best-fit model, with parameters listed in the top row of Table 2, reproduces all portions of the spectrum quite well, with few systematic deviations. The best-fit model is shown in Fig. 9 along with the higher signal-to-noise MEG data. In general, the continuum is well fit and the lines are adequately reproduced by this model. The same is true for the HEG data.

3.2. Time Variability and Spectral Analysis of the Pre-flare, Flare, and Post-flare Data

A large (factor of ~ 3) flare was seen in the middle of the *Chandra* observation, with a rapid rise of about six thousand seconds, followed by a steady decay during which the count rate drops by less than a factor of two in about 18 ks. After this, the count rate remains steady, but at a level that is nearly twice the quiescent, pre-flare level. The temporal behavior is shown in Fig. 10, where we also display light curves for the hard and soft bands separately. Significant hardening is seen during the flare, which dissipates through the flare and post-flare phase but never returns to the pre-flare level. We now discuss fits to separate spectra, formed from the pre-flare section of the observation, the flare section, and the post-flare section.

Table 2: APEC model fits

|	kT_1 (keV)	EM_1 (10^{53} cm^{-3})	kT_2 (keV)	EM_2 (10^{53} cm^{-3})	Abundance (Solar units[a])	$N_{\rm H}(ISM)$ (10^{22} cm^{-2})	$L_{\rm X}$ 10^{31} erg s^{-1}
total	$1.00^{+.04}_{-.03}$	$6.82^{+.82}_{-.69}$	$4.16 \pm .11$	$3.07^{+.06}_{-.07}$	$0.39 \pm .02$	$1.19^{+.03}_{-.04}$	5.44
pre-flare	$0.95^{+.05}_{-.06}$	$7.40^{+1.37}_{-1.19}$	$3.10^{+.14}_{-.13}$	$21.8^{+0.9}_{-1.1}$	$0.26 \pm .02$	$1.19^{+.03}_{-.05}$	3.49
flare	$1.58^{+.08}_{-.10}$	$18.1^{+4.3}_{-3.6}$	$7.81^{+2.22}_{-0.81}$	$40.5^{+1.9}_{-3.3}$	$0.43^{+.06}_{-.05}$	$1.18 \pm .05$	9.36
post-flare	$0.80^{+.09}_{-.05}$	$11.1^{+2.4}_{-1.6}$	$4.49^{+.24}_{-.50}$	$36.9^{+2.1}_{-1.6}$	$0.31^{+.05}_{-.04}$	$1.18^{+.06}_{-.05}$	6.78

[a]Solar abundances from (Anders & Grevesse 1989).
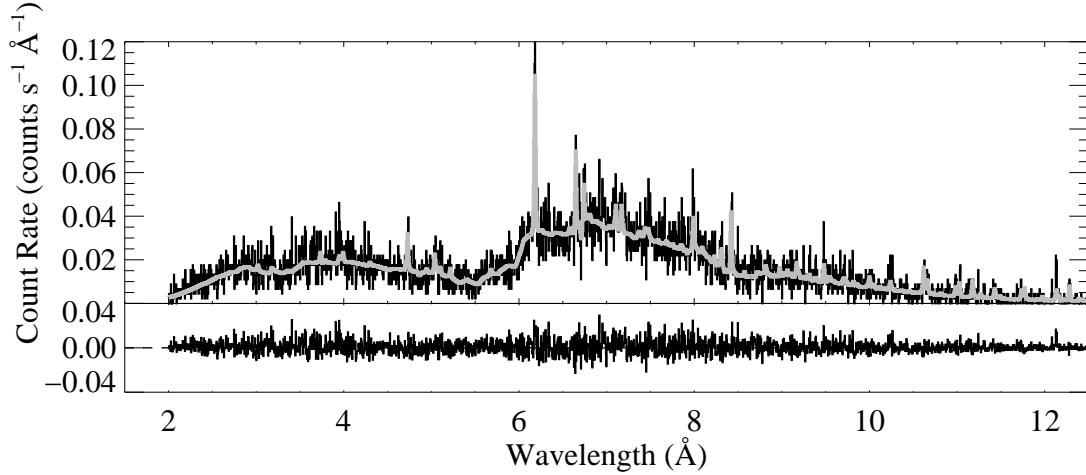
Fig. 9.— The best-fit two-temperature thermal emission model is superimposed (in gray) on the MEG data. Fit residuals are shown below each plot.
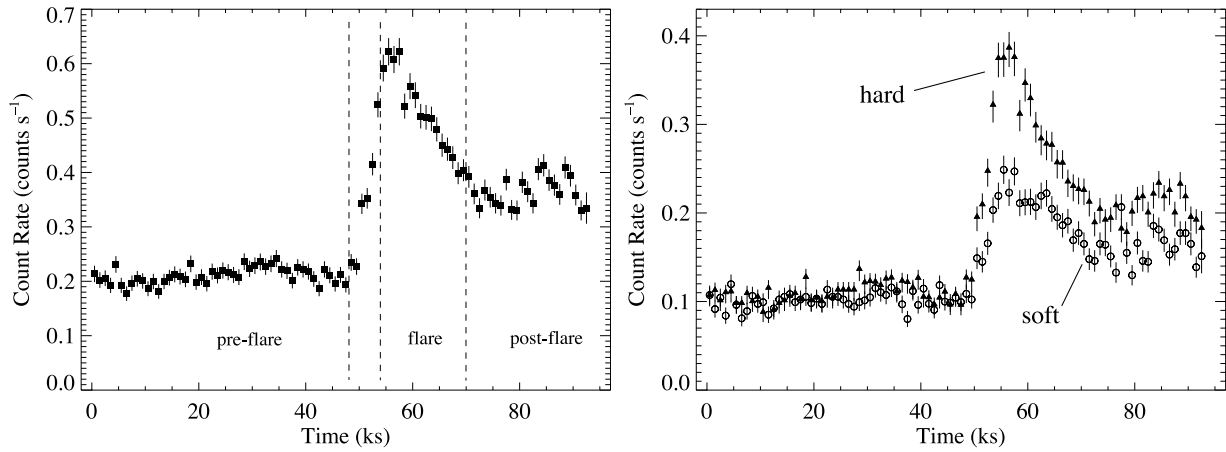

Fig. 10.— Left: A light curve with 1000 second bins formed from all counts in the dispersed, first-order spectra (both MEG and HEG) (left). Right: Light curves made from all counts with wavelengths longer than 6.8 Å (open circles) and shorter than 6.8 Å (filled triangles). The hardening of the emission during the flare is evident.

Above we have presented fits to the total spectrum collected during the 94 ks observation. We next repeat the two-temperature thermal fitting on the pre-flare (0 through 48 ks), flare (54 to 70 ks), and post-flare (70 to 94 ks) spectra separately. The results are reported in Table 2, and the temporal divisions are indicated by the vertical lines on the light curve in the first panel of Fig. 10. The temperatures and emission measures roughly double during the flare portion of the observation, with somewhat larger relative changes in the hotter component of the two-temperature model. The flare plasma temperature is in excess of 90 MK. The post-flare plasma also has a temperature distribution that is elevated with respect to the pre-flare plasma, indicating that some reheating is occuring. The absorption column densities derived for each section of the observation are completely consistent with each other, which is consistent with an interstellar origin to the attenuation, as we would expect. We also note that the abundances show a marginally significant change among the three different sectors of the observation, in the sense that the hotter components – the flare and to a lesser extent the post-flare sections – have higher abundances. Although this result may represent a real change in the coronal plasma abundances during the flare, it may also be affected by the simplified two-temperature assumption in the model. The abundance parameter in the emission model is largely controlled by the line to continuum ratio, and the relative strength of the metal emission lines to the bremsstrahlung continuum is also affected by details of the emission measure distribution at high temperatures, where metals are generally fully ionized and contribute little overall line emission.

Another demonstration of the spectral changes associated with the flare is provided by the iron K-shell line emission, which is sensitive to the hottest plasma. The He-like Fe XXV line complex near 1.86 Å has an emissivity that peaks near 60 MK, while the H-like Fe XXV line at 1.75 Å has an emissivity that peaks at temperatures somewhat above 100 MK. There is very little emission in these lines – and none detected in the H-like feature – during the pre-flare section of the observation. But the iron lines get significantly brighter during the flare and maintain significant emission levels during the post-flare phase, as well. The evolution of the HEG spectrum in the vicinity of these lines is shown in Fig. 11, along with the separate best-fit models for each of the three sections of the observation (these model parameters are listed in Table 2). Not only do the iron features increase in overall intensity during the flare, but the relative strength of the H-like feature compared to the He-like feature also increases, as is expected from the temperature increase seen in the APEC model fitting to the entire spectrum.
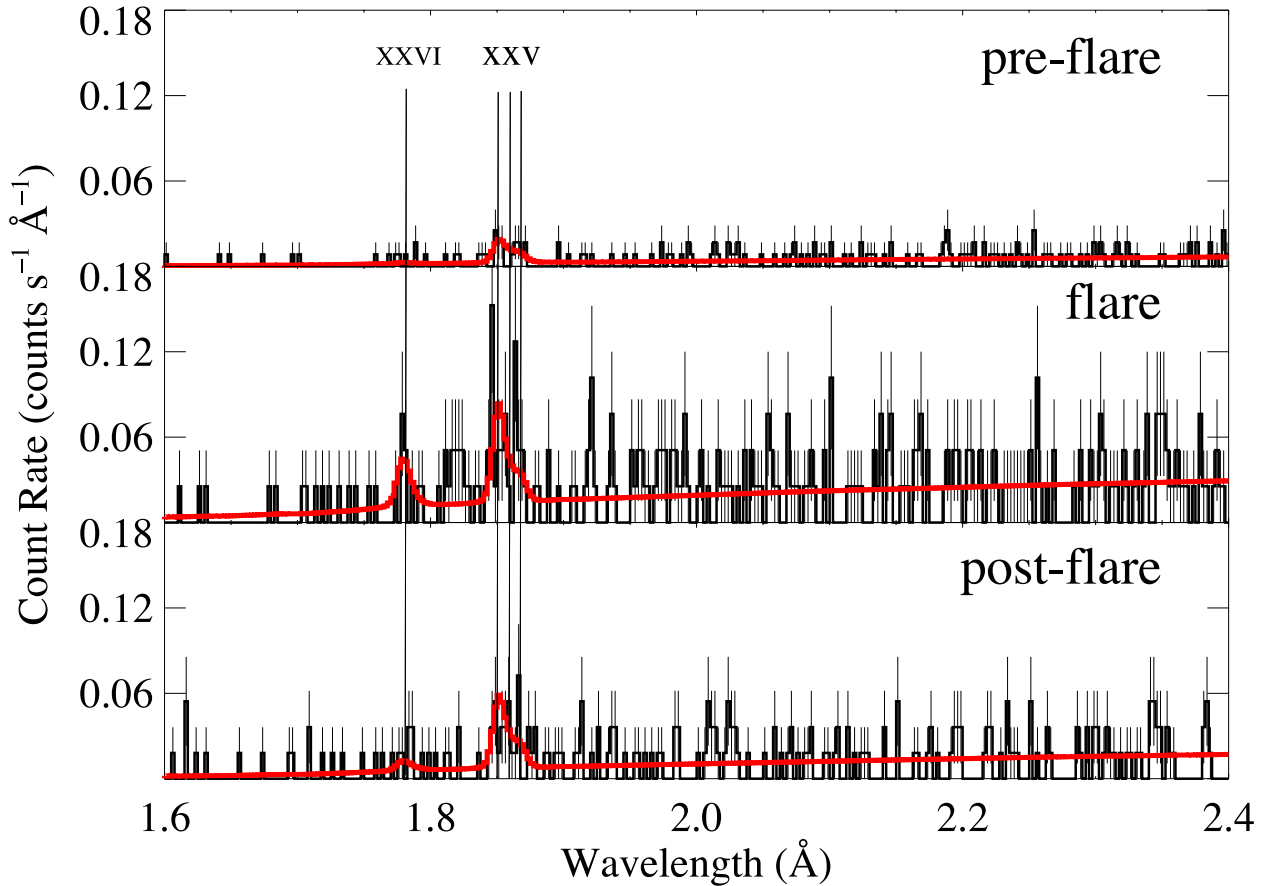
Fig. 11.— The evolution of the iron K-shell emission lines seen in the HEG spectrum. The Lyα line of Fe XXVI at 1.78 Å and the Heα line complex of Fe XXV near 1.86 Å (resonance, intercombination, and forbidden lines are individually indicated by the vertical lines) are plotted along with the nearby bremsstrahlung continuum. The best-fit model for each of the three separate sections of the observation are shown, superimposed on the corresponding spectral data. The increase in the plasma temperature during the flare (and sustained to a great extent through the post-flare section) is evident both in the change in the brightness of the iron lines and in the relative increase of the H-like line strength compared to the He-like line strength.

3.3. Density-Sensitive Emission Line Ratios

The emission lines in the spectrum are relatively weak, but we are able to analyze the strengths of several of the strongest ones, and use them as plasma diagnostics. Specifically, the forbidden-to-intercombination line ratios of helium-like ions are sensitive to density, as collisions de-populate the metastable upper level ^{3}S of the forbidden line, and populate the upper level ^{3}P of the intercombination line (Gabriel & Jordan 1969). Thus higher densities (with different critical densities for each element) decrease the forbidden-to-intercombination (f/i) ratio. This evidence for high densities is seen in some accreting T Tauri stars, but not in naked T Tauri or magnetically active main sequence stars (Kastner et al. 2002; Telleschi et al. 2007). *Probably should give a few more refs here. Eric, but the Telleschi reference summarizes several different results.*

We measured the line intensities by first fitting the continuum near each line complex as a flat spectrum, consistent with bremsstrahlung, and once the continuum level was established, we fit the line complex with a three Gaussian profile model on top of the best-fit continuum level. The adjustable parameters of the three Gaussian model are an overall normalization and the ratios $\mathcal{G} \equiv (f + i)/r$ and $\mathcal{R} \equiv f/i$. The f/i ratios for Si XIII and S XV are $5.4^{+2.6}_{-2.2}$ and $1.90^{+2.28}_{-.82}$, respectively. None of the lower atomic number elements have enough signal-to-noise in their helium-like emission complexes for a measurement to be made.

For the Si XIII, the ratio exceeds that low-density limit[4] of $f/i = 2.3$ to 2.5 with greater than one sigma significance. This limits the density to less than $\sim 10^{12}$ cm^{-3}, with a 95 percent upper confidence limit on the electron density of $4 - 9 \times 10^{12}$ cm^{-3}, depending on the model of $\mathcal{R}(n_e)$ that is employed. Our modeling of the line strengths does not explicitly include the Mg XII Lyman-β line that is blended with the Si XIII forbidden line. Given the strength of the Mg XII Lyman-α line, the Lyman-β line should only be about 10 percent as strong as the Si XIII forbidden line. Even if we allow for 20 percent given modeling uncertainties, that would bring the measured $\mathcal{R} = f/i$ ratio down to only about 4, and the conservative statistical upper limit of $n_e = 9 \times 10^{12}$ cm^{-3} would still correspond to the 68 % upper confidence limit. The HEG measurement of the line complex, along with the theoretical models from which we derive the upper limit on the density are shown in Fig. 12.

---

[4]The low density limit refers to the limiting (high) value of the f/i ratio that holds when the density is low enough that collisional excitation out of the metastable excited state of the forbidden line is unimportant compared to spontaneous emission to the ground state. We give a range of values for the low-density f/i limit for each element. These represent the range of values found from PrismSpect (MacFarlane et al. 2004) calculations, from Blumenthal et al. (1972), and from Porquet & Dubau (2000). If the actual electron density were much above the low-density limit, then the forbidden line would be weakened and the f/i ratio would be reduced.

For S xv the forbidden-to-intercombination ratio is consistent with the low-density limit for that complex of $f/i = 2.0$ to 2.1. The one sigma lower bound on f/i for S xv corresponds to a density of 10^{14} cm^{-3}. That the helium-like complexes on DoAr 21 have strong forbidden lines, consistent with being in the low-density limit, is in marked contrast to altered f/i ratios in accreting CTTS. However, the altered f/i ratios in CTTS are generally seen in lower Z elements' He-like complexes, such as Ne ix and O vii, which have lower critical densities than Si xiii. The lower Z features seen in those WTTS, which are at longer wavelengths, are not visible in the *Chandra* spectrum of DoAr 21 because of the large amount of interstellar attenuation. Nonetheless, the available density diagnostics for the X-ray emitting plasma of DoAr 21 are completely consistent with those seen for active, non-accreting coronal sources such as WTTS and ZAMS stars.
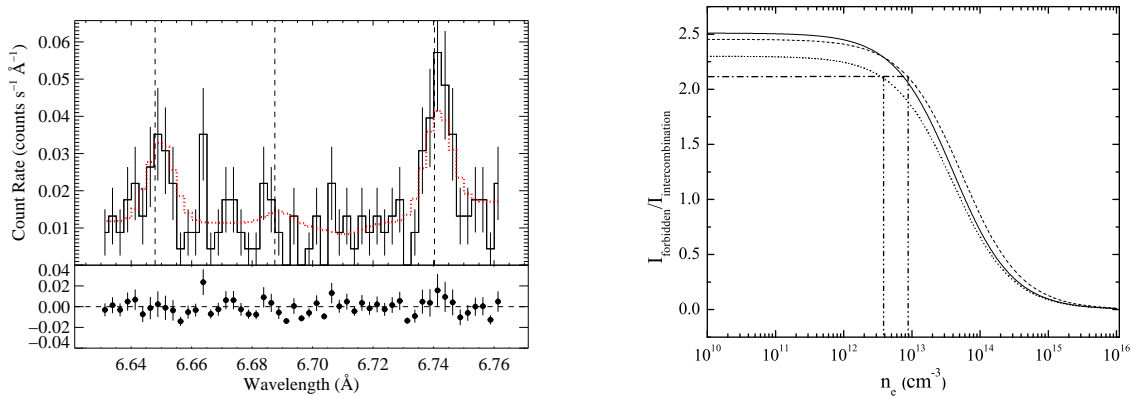
Fig. 12.— The Si XIII in the HEG (left) shows a strong forbidden line (at 6.74 Å) and a weak intercombination line (at 6.68 Å), consistent with the low-density limit. Models of the f/i ratio of Si XIII (right) as a function of electron density. The models are from Blumenthal et al. (1972) (solid curve), Porquet & Dubau (2000) (dotted), and PrismSpect (MacFarlane et al. 2004) (dashed). The horizontal dash-dot line represents the 95 % lower confidence limit of $f/i = 2.10$. Depending on which of the three models are used, this value corresponds to an electron density of $n_e = 4 - 9 \times 10^{12}$ cm^{-3}.

4. Discussion

Our X-ray observations show DoAr 21 to be a very active, hard, coronal source, with a large X-ray luminosity and flare rate. At the same time, our new infrared observations of DoAr 21 show the presence of extended, irregularly distributed circumstellar material. In light of this combination, we now consider the relationship between DoAr 21's radiation and its circumstellar environment, and what it can tell us about DoAr 21's evolutionary state and more generally about disk evolution around young stars.

Much of what we can learn from these data rests on where exactly the circumstellar material is located, and how it is related to DoAr 21. Is it the remnant of a disk that is in the final stages of being cleared out? Or is it nearby but not necessarily gravitationally-bound material that is illuminated by DoAr 21 as it emerges from or passes through the cloud? Is some of the material that we see projected near DoAr 21 perhaps in the foreground or background?

We divide the discussion into two major parts. First, we consider the emission mechanism and energetics of the observed infrared emission (including the H_2 and PAH emission) from the circumstellar material; as a corollary to this we evaluate further literature data bearing on DoAr 21's level of stellar activity, and we use it to estimate the far-ultraviolet (FUV) radiation field. We then discuss possible origins for this circumstellar material, focusing in particular on whether or not it is a disk, i.e. gravitationally bound, centrifugally supported material.

4.1. Energetics and excitation of the circumstellar material

The most surprising result from the new observations presented here is the large spatial extent of the mid-infrared emission from DoAr 21, which is puzzling to find around a cool star, and one with a very low millimeter flux. What this discovery has in common with the previous surprises about DoAr 21—the detections of PAH and H_2 emission—is that all of these observations are more commonly associated with more luminous, hotter stars. Here we explore whether it is possible to construct a model that explains all of the data, and we focus in particular on trying to understand the influence of the UV and X-ray emission from DoAr 21 on its circumstellar material. Because FUV radiation is important for radiative excitation of both H_2 and PAH emission, we first discuss the FUV radiation field near DoAr 21.

4.1.1. The FUV radiation field near DoAr 21

The ultraviolet flux from DoAr 21 is poorly known. It was not detected by IUE (Valenti et al. 2003); examination of the archived IUE spectrum places a rough upper limit of $\sim 10^{-15}$ erg cm^{-2} s^{-1} at $\lambda = 2400$–3200 Å. Given the large extinction to DoAr 21 (roughly 13 magnitudes at $\lambda = 2400$ given our adopted visual extinction), however, the star could have an ultraviolet flux that is several orders of magnitude above its photospheric flux and it would not have been detected by IUE. Given this situation, we take two approaches to estimating the level of UV radiation in the vicinity of DoAr 21. First we consider the UV background in the region due to the nearby B2 star HD 147889. Then we use the available data on DoAr 21's chromospheric and coronal activity to estimate the UV emission from its transition region.

The B2 V star HD 147889, at a projected distance of 0.4 pc from DoAr 21, is responsible for exciting PAH and H$_2$ emission from much of the surrounding nebulosity (Habart et al. 2003). To determine the UV flux from HD 147889 arriving at the position of DoAr 21 and its surroundings, we integrated the flux from a synthetic spectrum based on a spherical, hydrostatic, class (ii) NLTE model atmosphere from Aufdenberg et al. (1999) with $T_{\rm eff} = 22000$ K and $\log g = 3.9$, assuming $L = 5300\ L_{\odot}$ for HD 147889 and a distance of 0.4 pc between the two stars (Liseau et al. 1999). At this distance, the ultraviolet flux reaching DoAr 21 from HD 147889 (assuming no attenuation) is roughly 0.75 erg cm^{-2} s^{-1} in the bandpass 6.0–13.6 eV ($\lambda = 912$–2066 Å). This corresponds to $G_0 \approx 470$, the flux expressed in units of 1.6×10^{-3} erg cm^{-2} s^{-1} (Habing 1968)[5]. In contrast, the FUV field from DoAr 21's photosphere (estimated using a Kurucz model atmosphere and the stellar parameters given above) is $G_0 \approx 0.075$ at a distance of 1 $R_{\star}$ from the stellar surface and falls with distance from DoAr 21. As noted above, however, given the high level of activity from DoAr 21, there is likely to be significant UV emission from the transition region.

To estimate the FUV flux from DoAr 21, we use as a template HD 2832572 (V987 Tau), a weak-lined T Tauri star with a similar mass, effective temperature, and X-ray properties. HD 2832572 is a single G5 star in the Taurus-Auriga star-forming region, and it has an X-ray luminosity of $L_X = 1.1 \times 10^{31}$ erg s^{-1} in the 0.3–10 keV band (Telleschi et al. 2007, scaled to the 129 pc distance measured by Torres et al. 2007). DoAr 21's luminosity in this energy band (averaging over our whole observation, i.e. over both flare and quiescent states) is $L_X = 5.4 \times 10^{31}$ erg s^{-1}. HD 2832572 is near DoAr 21 on the HR diagram, although with a slightly hotter photospheric temperature and older inferred age; it is the second blue square from the left in Figure 1. It has no evidence for circumstellar dust (Furlan et al. 2006;

---

[5]This is the same quantity referred to as χ by Habart et al. (2003)

Kundurthy et al. 2006) or H_2 (Bary et al. 2003). It shows a hard, flaring X-ray spectrum (Favata, Micela, & Sciortino 1998); fitting of the spectrum yields a temperature distribution similar to what we find for DoAr 21 (Telleschi et al. 2007). Like DoAr 21, it shows strong radio emission (Phillips, Lonsdale, & Feigelson 1991).

These similarities make HD 2832572 a good template to compare with DoAr 21, along with the crucial difference: it has a relatively low $A_V = 0.4$ mag (Furlan et al. 2006). Thus, the FUV emission is not attenuated nearly as much as for DoAr 21, and the star was clearly detected by IUE. We integrated the de-reddened FUV flux in the HD 2832572 IUE spectrum in the range $\lambda = 1150$–2066 Å. The Ly α line is clearly contaminated by geocoronal emission; we estimated by eye that approximately 2/3 of the line is geocoronal and rejected this flux.[6] Since the $\lambda = 912$–1150 Å flux was not observed by IUE, we used the results of Alexander, Clarke, & Pringle (2005), who used detailed differential emission measure distributions for several T Tauri stars and found that the $\lambda = 912$–1150 Å flux was roughly 20% of the $\lambda = 912$–2000 Å flux; thus, we scaled the de-reddened IUE 1150–2066 Å flux by 1.2 to estimate the flux in the full 912–2066 Å interval. We used the measured distances of HD 2832572 and DoAr 21 (both with high-quality VLBA parallaxes) to determine the scaling between flux and luminosity for both stars. Finally, we scaled the HD 2832572 FUV luminosity by the two stars' relative L_X values to estimate the DoAr 21 FUV luminosity, assuming that the FUV luminosity would be directly proportional to the X-ray luminosity.

Based on this analysis, we find $L_{\rm FUV} \approx 2.3 \times 10^{32}$ erg s^{-1}. Thus, G_0 from DoAr 21 is ≈ 2800 at $1\rlap{.}''1$ (134 AU) from the star, the distance of the bright ridge in our images. Thus, the estimated FUV flux from the star is significantly greater than the external FUV flux at this distance. The total FUV flux (from the combined transition region and B2 star background) at the position of the bright ridge is $G_0 \approx 3300$; the two fluxes become equal at ~ 330 AU from DoAr 21.

Having estimated the FUV flux near DoAr 21, we can now examine the effect this flux would have on nearby material. We examine in turn the continuum (dust) emission, the PAH emission, and the H_2 emission. Consistent with the FUV flux estimates above, we will show that the emission show signatures of being excited from the inside out, i.e. by DoAr 21 rather than externally by HD 147889.

---

[6]If we reject the flux in the contaminated line center entirely, which is clearly an overcorrection, the estimated G_0 from DoAr 21 decreases by a factor of roughly 2.6.

4.1.2. Dust emission

In order to study the continuum emission excess from DoAr 21, which we here assume arises from thermal emission from dust grains, we need wavelength regions without significant spectral features. The spectrum taken by Hanner, Brooke, & Tokunaga (1995) shows that the region encompassed by the 10.4 μm filter from our Gemini observations is free of emission or absorption features; in particular, there is no evidence of a silicate feature. While we do not have a corresponding spectrum in the 18.3 μm region, this part of the spectrum generally has not shown significant features in Spitzer IRS spectra of other young stars (Geers et al. 2006). Some galaxies and star-forming regions with PAH emission do show features at 17.8 μm and 18.9 μm, albeit on top of a significant continuum (Sellgren, Uchida, & Werner 2007). We take this spectral region to sample primarily continuum emission; if there is a contribution from some PAH emission in this bandpass, the effect would be to raise the dust temperatures derived below.

Using our Gemini images, we integrated the flux in these two bandpasses in regions that are off the stellar position and thus probe only circumstellar flux. This yielded fluxes of 197 and 603 mJy at 10.4 and 18.3 μm, respectively. A single-temperature blackbody fit to these two fluxes yields a temperature estimate of roughly 215 K for the emitting material. While this estimate is obviously an oversimplification of the actual situation, the general result of a steeply-rising flux from 10–18 μm is robust, indicating that the emitting material has a temperature in the hundreds of degrees K. For comparison, blackbody grains that have reached thermal equilibrium with the star's radiation field, given DoAr 21's luminosity of 11.7 $L_\odot$, would have a temperature of 44 K at 135 AU (1$''$1) from the star and 31 K at 270 AU from the star. At these temperatures, the 18.3 μm to 10.4 μm flux ratio would be 10^5–10^7, rather than the observed value of ~ 3.

While the derived dust temperature is far out of equilibrium, it is quite consistent with the expected behavior for very small grains (VSGs) excited by UV photons (Puget & Leger 1989). Grains with radii of a few nm can be transiently heated to temperatures of several hundred K by single UV photons and an ensemble of such grains can contribute significant infrared emission. Given that such small grains may form a continuum of sizes with PAH molecules (Tielens 2008), it is perhaps not surprising to find them around DoAr 21. Nevertheless, it provides additional evidence for the importance of the FUV radiation in exciting the circumstellar material, and it is another respect in which DoAr 21's environment is different from a typical circumstellar disk.

4.1.3. PAH emission

We have presented our new images in the 8.6 and 11.3 μm PAH filters above; here we briefly recap existing published and archival PAH data for DoAr 21.

Figure 6 shows the mid-infrared spectrum of DoAr 21 from Hanner, Brooke, & Tokunaga (1995) along with the model photosphere. The data show a clear emission feature at $\lambda = 11.25$ μm, attributed by Hanner, Brooke, & Tokunaga (1995) to emission from PAHs. The data also show a rising slope shortward from $\lambda = 8.5$ μm to where the spectrum ends at 7.9 μm, consistent with the presence of a 7.7 μm PAH emission feature.

DoAr 21 was also observed by ISO with the circularly-variable filter (CVF) on ISOCAM, yielding a $\lambda/\Delta\lambda \approx$ 50–80 spectrum from 5.1–16.6 μm of DoAr 21 and its surroundings with 6$''$ pixels. These data were reprocessed by Boulanger et al. (2005) as part of the final reprocessing of all ISOCAM CVF data, and we retrieved the reprocessed data from the ISO archive. The data show a strong point source at the position of DoAr 21, as well as a bright ridge of emission located 30$''$–90$''$ NE of DoAr 21 and running NW–SE; this ridge is clearly visible in the *Spitzer* 24-μm image as well (Figure 3; see also Figure 3 of Padgett et al. 2008 for a larger view) and can also be seen faintly in the 2MASS K-band images. All pixels in the ISOCAM 3$.\!\!'$3 x 3$.\!\!'$3 field of view show a rich PAH spectrum, including emission features at 6.2, 7.7, 8.6, 11.3, and 12.7 μm.

Unfortunately, it is not possible to determine a reliable spectrum for DoAr 21 itself from these data. Due to internal reflections in ISOCAM when used with the CVF, the spectrum of DoAr 21 is contaminated by "ghosts", reflections of stray light from elsewhere in the field of view (Okumura et al. 1998). This is revealed by sharp discontinuities in the spectrum around 9 μm, the transition wavelength between CVF1 and CVF2. The ghosts are significantly worse in CVF2, and this discontinuity (which is clearly present in a spectrum extracted at the position of DoAr 21) is a signature of stray light contamination (Boulanger et al. 2005). We suspect that the contamination arises from the bright ridge of emission to the NE of DoAr 21, which is of the same order of magnitude in brightness at these wavelengths as DoAr 21 itself. Because the background emission is diffuse and spatially variable, and the ghost size and strength are functions of wavelength, it is not possible to reconstruct the uncontaminated spectrum of DoAr 21 from these data.

One of the most striking features of our new PAH-filter images of DoAr 21 is the spatial variation of the 11.3 μm emission, with similar variations seen at 18.3 μm. The emission does not decrease smoothly with distance in the region near the star, but rather it is significantly brighter in a knot and partial arc beginning roughly 1$.\!\!''$1 to the north and west of the star. In contrast, the 8.6 μm emission is much smoother, with about the same brightness in the

region near that star as in the region that appears as a bright arc in the 11.3 μm image. Thus, it appears that the [8.6]/[11.3] ratio may be higher near the star. However, the 8.6 μm emission is much fainter overall than the 11.3 μm emission, and the star is brighter, so it may be that any variation in the fainter 8.6 and 10.4 μm emission blends in with the wings of the stellar PSF.

If the apparent change in the [8.6]/[11.3] ratio is real, it is a useful diagnostic of the ionization state of PAH molecules; in laboratory spectra of PAH molecules, the 11.3 μm CH out-of-plane bending mode weakens considerably in ionized PAHs while the 8.6 μm CH in-plane bending mode strengthens somewhat (Allamandola, Hudgins, & Sandford 1999). In astrophysical sources, a decrease in the [8.6]/[11.3] ratio with distance from a central ionizing source has been observed in NGC 1333 (Joblin et al. 1996) and in the Orion Bar (Galliano et al. 2008).

Applying this interpretation to DoAr 21 leads to the conclusion that a significant fraction of the PAH molecules with about 1″ of the star are ionized, suppressing the [8.6]/[11.3] ratio in this region. This would indicate that DoAr 21, not HD 147889, is the dominant source of FUV flux in its circumstellar environment, consistent with our estimates above of the relative FUV fluxes (Sec. 4.1.1). The first ionization potential for typical PAH molecules is 6–8 eV (Weingartner & Draine 2001b), and thus there must be significant flux in this band near the star.

As noted above, it may be that a similar spatial variation in the faint 8.6 μm emission is simply difficult to detect due to the low surface brightness. One piece of evidence in favor of this interpretation is that the bright 18.3 μm emission shows the same spatial variation as the bright 11.3 μm emission, while the fainter 10.4 μm emission apparently does not. Since both the 10.4 and 18.3 μm bands are dominated by continuum emission from very small grains, they should show the same spatial variation. If it is the case that the same radial variation is present in all bands, then it would represent a real change in surface density of material, with less material present near DoAr 21. In either case, the azimuthal distribution of material around DoAr 21 is clearly asymmetric (Fig. 5).

While there is a sharp increase in the 11.3 μm emission at roughly 1″1 from the star, the brightness of this emission declines with radial distance beyond that point. The decline is roughly consistent with a falloff proportional r^{-2}, which is what would be expected from a uniform PAH and small grain surface density with declining excitation due to geometric dilution of the exciting radiation. Thus, the true extent of the circumstellar material may be much greater than that shown in our images.

4.1.4. H_2 emission

While we did not make any observations of H_2 emission, the analysis of the VSG and PAH emission in the preceding sections bears directly on the interpretation of previous H_2 observations, which we discuss here. Given the surprisingly large spatial extent of the emission seen in our images, we pay particular attention to what constraints existing data put on the spatial distribution of the H_2 emission.

As noted above, Bary et al. (2002, 2003) detected emission in the H_2 1–0 S(1) line at $\lambda = 2.12$ μm from DoAr 21. Their slit width was $0\rlap{.}''8$ and the seeing was approximately $1\rlap{.}''4$ (Bary et al. 2002). In their nod-differenced images, they found no evidence of any extension of the emission along the E-W slit beyond the $1\rlap{.}''4$ seeing disk. From the resolved velocity width of the line, they also argued that the gas must reside in a rotating circumstellar disk.

Bitner et al. (2008) observed DoAr 21 in the 0–0 S(2) pure rotational transition of H_2 at $\lambda = 12.279$ μm. They detected emission in one observation using a $1\rlap{.}''4$ N-S slit with $1\rlap{.}''4$ seeing on the IRTF, but they did not detect it in a subsequent observation with a $0\rlap{.}''54$ E-W slit with $0\rlap{.}''5$ seeing on Gemini. (FWHM seeing profiles and slit orientations are from M. Bitner, personal communication.)

The Bitner et al. (2008) observations suggest that the S(2) H_2 emission is not uniformly distributed around the star and/or is time-variable. If we attribute the difference between the two observations solely to the spatial distribution of material, the data imply that the emitting gas lies primarily at an angular separation greater than $0\rlap{.}''25$ (30 AU), and that it may be more concentrated to the N and/or S of the star. Bitner et al. (2008) detected larger fluxes with the wider IRTF slit than with the narrower Gemini slit for four out of the five sources observed with both telescopes, suggesting that spatially-extended emission for the pure rotational transitions is not uncommon. We note, however, that a slit at any orientation will intercept flux from a disk at all disk radii (though not all azimuths), so azimuthally-symmetric emission from gas in a disk, even at large radii, should contribute some flux even in the Gemini slit. We discuss this point further in Sec. 4.2, where we propose a possible geometry for the emitting material that is consistent with all the data.

The suggestion that the H_2 S(2) emission may lie preferentially to the N or S, combined with the emission geometry seen in our PAH images, suggests that the H_2 and PAH emission could be coincident, and other observations suggest that this is not an uncommon occurrence. This is perhaps unsurprising, given that both molecules are excited by UV photons. In the Orion Bar PDR, the H_2 1–0 S(1) emission and 3.3 μm PAH emission are similarly distributed

along the edge of the bar facing the ionizing O stars.[7] Closer to DoAr 21, Gómez et al. (2003) and Habart et al. (2003) conducted ground-based narrow-band imaging, showing that the SW edge of the bright bar lying NE of DoAr 21 (seen in both the *Spitzer* and ISO images) is also bright in the H_2 1–0 S(1) line. Further, Habart et al. (2003) show that the PAH emission seen by ISOCAM at $\lambda = 5$–8.5 μm in this region correlates very well in strength and position (albeit with modest spatial resolution) with the H_2 1–0 S(1) emission seen in the ground-based images, and with the H_2 0–0 S(3) emission seen by the ISO SWS.

An alternate interpretation of the Bitner et al. (2008) observations is that the emission is time-variable and was below the detection threshold at the time of the Gemini observation. The 3σ upper limit in the Gemini observation is 1.25×10^{-15} erg cm^{-2} s^{-1}, a factor of 2.6 below the flux level of the IRTF detection.[8] The X-ray flux level from DoAr 21 is seen to vary by a factor of three on short timescales (Fig. 10); if this translates into a corresponding variation in the FUV exciting the H_2 emission, then that emission could vary by similar factors. If we attribute the difference between the two observations solely to variability, this hypothesis would require, however, that the Bitner et al. (2008) detection happened to coincide with the peak of a flare, and that the H_2 flux in the Gemini observation is just below the detection threshold. DoAr 21 has a relatively high X-ray flare rate of about one per day (Imanashi et al. 2002), but the fraction of time the X-ray flux is more than a factor of 2.6 above the quiescent level is small, probably less than an hour per day based on available data.

4.1.5. Photometric and Polarimetric Variability

Multiple measurements exist at wavelengths from 0.39 μm (U) through 4.8 μm (M). Variability is seen at all wavelengths. The range at V band in 15 measurements is 0.33 magnitudes, with variations on timescales of less than one day, but with no apparent periodicity (Bouvier et al. 1988). Substantial variability is seen in the ultraviolet; in two observations separated by less than an hour, Bouvier et al. (1988) observed a brightening of 0.97 magnitudes in U, while B brightened by 0.03 magnitudes and V faded by 0.02 magnitudes. Two observations separated by 3 hours on the following night showed a similar variation, with U

---

[7]While to our knowledge there is not a similar map of the 11.3 μm line in the Orion Bar, the 3.3 μm PAH line is strongest in neutral PAHs and in general is strongly correlated with the 11.3 μm line (Hony et al. 2001).

[8]This limit is determined using the line width of 5.6 km s^{-1} measured in the IRTF observations (M. Bitner, personal communication), and thus it is slightly lower than the limit given in Bitner et al. (2008) based on an assumed line with of 10 km s^{-1}.

brightening by 0.42 magnitudes while B and V faded by 0.04 and 0.05 magnitudes, respectively.[9] Such a large increase in the UV emission without a concurrent increase in V cannot be due to rotational modulation (either of hot or cool spots), since that would increase the flux in all bands (e.g., Rydgren & Vrba 1983). These U-band brightenings are similar to flares seen on active main-sequence stars in that they are much brighter at U than at V (Fernández et al. 2004). We note that both of these brightening events occur when the star is at the faint end of the observed U range, i.e. they are brightenings toward the mean value rather than above it. This may simply indicate that the star is flaring much of the time and that the observed mean value in the data of Bouvier et al. (1988) is characteristic of the flares rather than the photosphere; this is consistent with the fit to the SED (Figure 2). The U and B magnitudes are positively correlated with each other (with a larger amplitude at U), but neither the U or B magnitudes nor the $U - B$ color is correlated with V.

The bluest observed $U - B$ color for DoAr 21 in the photometry of Bouvier et al. (1988) is $U - B = 0.5$, observed on two consecutive nights. Using our adopted extinction, the de-reddened color is $(U - B)_0 \approx -0.7$. This has a color temperature of $T \approx 17,000$ K (Aller et al. 1982), significantly hotter than the star's photosphere and than the 8,000–11,000 K temperatures typically deduced for accretion-related veiling emission in classical T Tauri stars from optical or ultraviolet spectra (e.g., Valenti, Basri, & Johns 1993).

DoAr 21's K-band emission is polarized at $p \approx 2\%$ (Martin et al. 1992). The large visual extinction toward DoAr 21 suggests that this could be attributed to interstellar polarization from overlying cloud material not closely associated with the star. However, the polarization is variable both in amplitude and in position angle (Jensen et al. 2004). Since a cloud far in the foreground would not be expected to change on short timescales, this variability suggests a circumstellar origin for DoAr 21's polarization; this is also quite consistent with the observed asymmetry of the circumstellar material, as scattering off an asymmetric distribution will give a net polarization in the unresolved light. Given the discovery reported here that the circumstellar material around DoAr 21 is quite extended (Sec. 2.3.2), the observed variation in polarization percentage could be due to measuring with different aperture sizes that include different amounts of the extended emission: the percentage polarization measured by Jensen et al. (2004) in a 4″.3-diameter aperture is smaller than that measured by Martin et al. (1992) in a 7″.8 aperture.

---

[9]Bouvier et al. (1988) do not give error bars on individual measurements. They quote typical errors of 0.09, 0.06, and 0.04 mags for U, B, and V for a $V = 12$ star; DoAr 21 is $V \approx 14$. Observations of other stars with similar V magnitudes observed during the same nights as the U flares on DoAr 21 do not show U magnitudes that are substantially different from the mean values for those stars, suggesting that the observed changes at U in DoAr 21 are real, and not photometric errors.

4.2. A Disk, or Not?

What is strikingly clear from the observations presented above is that the high-energy emission from DoAr 21 has strong interactions with material in its circumstellar environment, even on scales of hundreds of AU. What is less clear, however, is the relationship of the observed material to DoAr 21, and specifically to what extent the extended emission is related to any orbiting, bound circumstellar (or circumbinary) disk that DoAr 21 has or once had.

The definitive answer to this will await further, higher-resolution observations, in particular, spatially- and velocity-resolved mapping of the H_2 emission. Here, we close the discussion with an examination of evidence for and against a Keplerian disk around DoAr 21.

One of the primary arguments that Bary et al. (2002) made for the H_2 emission arising from a disk is that extended, non-disk material would have a narrower line width than the 9 km s^{-1} FWHM width they observed for DoAr 21's 1–0 S(1) emission. While we examine this line width more quantitatively below, we first note that DoAr 21 has the narrowest H_2 line of any of the detections of H_2 from T Tauri stars and Herbig Ae/Be stars at both 1–0 S(1) (Bary et al. 2003; Itoh et al. 2003; Takami et al. 2004; Ramsay Howat & Greaves 2007; Bary et al. 2008; Beck et al. 2008) and 0–0 S(2) (Bitner et al. 2008).

To interpret the line width, we must take into account the spectral resolution. The Bary et al. (2002) observations had a FWHM spectral resolution of 5 km s^{-1}. Assuming Gaussian profiles for the spectral response and the observed line, the intrinsic line width is then 7.5 km s^{-1}. If interpreted solely as a thermal line width, this would imply a kinetic temperature of 2450 K. Bary et al. (2002) do not quote an uncertainty for the measured line width; assuming a 1 km s^{-1} total uncertainty for the deconvolved line width (reflecting some uncertainty in both the measured line width and the spectral resolution), the range of derived kinetic temperatures is then 1700–3300 K. The lower end of this temperature range is quite consistent with temperatures generally found for 1–0 S(1) emitting gas. For example, Bary et al. (2008) quote a standard thermal excitation temperature of 2000 K. Beck et al. (2008) observed extended H_2 around several T Tauri stars, and from the ratios of several lines they derive LTE temperatures of 1800–2300 K for H_2 around T Tauri stars. While the gas in many of those sources may be shock-heated, which is unlikely for DoAr 21, this result does show that H_2 can survive and emit strongly at the temperatures necessary to explain the observed line width in DoAr 21. Similarly, the models of Nomura & Millar (2005) and Nomura et al. (2007) predict that the bulk of the H_2 1–0 S(1) emission from disks irradiated by X-rays and UV comes from gas with temperatures of 1000–2000 K, and similar results are found in models of PDRs (Allers et al. 2005). Thus, the H_2 temperature necessary

to explain DoAr 21's observed line width solely with thermal broadening is consistent both with theoretical expectations and with observations of other sources.

Theoretical models show that it is plausible that DoAr 21 can heat gas to these temperatures at large distances from the star. The FUV flux that we estimate for DoAr 21 (Sec. 4.1.1) combined with HD 147889 corresponds to $G_0 \approx 3300$ at a distance of 130 AU ($1''1$) from DoAr 21, the location of the bright PAH emission ridge. This is similar to the FUV flux in the Nomura & Millar (2005) models at a radius of ~ 50 AU, and thus we might expect conditions at 130 AU from DoAr 21 to be similar to those at 50 AU in the models. This radius is slightly larger than the ~ 30 AU distance at which the H_2 1–0 S(1) emission peaks in those models, but it is also the case that DoAr 21 has an X-ray luminosity that is 50 times larger and a spectrum that is much harder than that assumed in these models, thus contributing an additional source of heating. Thus, while the models do not apply directly to DoAr 21, plausible scaling from them suggests that H_2 at > 100 AU from DoAr 21 could have $T > 1000$ K, necessary to produce the observed line width with thermal motions, and could emit at the observed level, since the predicted H_2 flux in both the 1–0 S(1) and rotation lines in these models is similar to that observed for DoAr 21.

To summarize this part of the discussion, the primary argument of Bary et al. (2003) for the presence of a disk around DoAr 21 is essentially that the only way to produce the observed H_2 1–0 S(1) line width is from rotation in a disk. However, we have shown that the observed width is a plausible thermal line width for H_2 illuminated with a strong FUV and X-ray flux, and that the flux from DoAr 21 is sufficient to produce the necessary heating at distances of ¿ 100 AU from the star, consistent with the position of the observed PAH and VSG emission. While the match between this expected thermal broadening and the observed line width does not rule out the gas also having some bulk motion, for example from rotation in a disk, it does show that rotation is not required to explain the data. Indeed, the observed line width sets some significant limits on the $v_{\mathrm{orbit}} \sin i$ of the gas. The expected Keplerian velocity of gas orbiting a 2.2 $M_\odot$ star at 130 AU is 3.8 km s^{-1}. Given the uncertainties in the range of possible temperatures for the emitting gas, such an orbital velocity is likely allowed by the data for any $\sin i$. Orbiting gas at significantly smaller radii, however, would require values of $\sin i$ significantly less than one.

As noted above, the two measurements of H_2 from DoAr 21 Bitner et al. (2008) gave different results, suggesting that the bulk of the 0–0 S(2) emitting gas lies to the north or south of the star. However, the 5.6 km s^{-1} FWHM of the S(2) line suggests that this gas is not coincident with the gas detected by Bary et al. (2002) in the 1–0 S(1) line. In general the S(2) line traces cooler gas, so the Bitner et al. (2008) observations may be tracing gas that is somewhat farther from DoAr 21 than the Bary et al. (2002) observations.

We have presented above a large body of data on DoAr 21, some of it seemingly contradictory. To close we present here a broad picture of DoAr 21's circumstellar environment. This is not the only possible scenario, but we suggest that it is consistent with all of the available data, and it is testable with future observations. In this scenario, DoAr 21 no longer possesses any substantial orbiting circumstellar material, either in the form of gas or dust. Either the system never had much of a disk (possibly as the result of the formation of the binary companion), or the extreme FUV and X-ray luminosity have photoevaporated the disk. The excess infrared emission, as well as the H_2 emission, comes from the extended material seen in our Gemini images, at hundreds of AU from the star. This material may be molecular cloud material that is not directly associated with the formation of DoAr 21; DoAr 21 may simply have moved into the vicinity of this gas because of its motion through the cloud. The FUV flux from DoAr 21 has created a small-scale PDR in this nearby gas, exciting the observed H_2, PAH, and VSG emission. As in models of PDRs Allers et al. (2005), the 1–0 S(1) emission is at the edge of the PDR and extends farther into the ionized region, explaining why Bary et al. (2002) detect some emission in an E-W slit that does not intersect the bright ridge to the north, but Bitner et al. (2008) do not detect emission in a transition that traces cooler gas.[10]

One major testable prediction of this scenario is the spatial distribution of H_2 emission. This could be mapped with narrow-band filters, or (ideally) with an integral-field spectrograph that would also measure the line widths and line ratios to probe the physical conditions in the emitting gas. For example, observations of both the S(1) 1–0 and the S(1) 2–1 lines would probe whether the gas is predominantly thermally excited or pumped by FUV photons.

Spatially-unresolved observations at high spectral resolution should detect more flux in a N–S slit than in an E–W one; making observations close in time with different slit orientations would help determine whether time variability or spatial distribution is more important. Given that PDR models predict that 1–0 S(1) emission is spread over a range of emitting temperatures, the 1–0 S(1) line measured in a N–S slit may have a stronger flux and a somewhat narrower width than the line observed by Bary et al. (2002) as it may sample both hotter and cooler gas. In contrast, if there is a Keplerian disk that produces the 1–0 S(1) emission, as suggested by Bary et al. (2002), then closely-spaced observations with different slit orientations should produce the same flux and line width, and mapping of the line emission should show it closely associated with the stellar position of DoAr 21.

---

[10]While the bright spot $1\rlap{.}''1$ to the N lies outside the slit used by Bary et al. (2002), if we assume a Gaussian profile for the seeing with $1\rlap{.}''4$ FWHM, then roughly 12% of the flux of a point source $1\rlap{.}''1$ away from the star would fall within the slit, so the northern ridge could still make some contribution to the observed flux.

To close, we note that the strong PAH emission at large distances from DoAr 21, and the implied strength of the FUV flux needed to excite it, lends empirical support to the hypothesis of Alexander, Clarke, & Pringle (2005) that there may be significant FUV flux from T Tauri stars even after accretion has ceased. Such a flux might enable photoevaporation to disperse outer disks on a short timescale even after accretion from the inner disk ceases.

5.   Conclusions

We have presented a variety of new data on DoAr 21 in an attempt to understand its circumstellar environment and the influence of high-energy radiation on it. High-resolution mid-infrared images show PAH and very small grain emission in an irregular distribution over hundreds of AU from the star, with little emission from the inner 100 AU where a circumstellar disk might lie. A new high-resolution X-ray grating spectrum from *Chandra* reveals a very luminous, hard corona, dominated by plasma at 10^8 K; neither this spectrum nor a new high-resolution optical spectrum shows any evidence for accretion. The inferred FUV radiation from the transition region of DoAr 21 is strong enough to excite the observed PAH, VSG, and H_2 emission, creating a small-scale PDR around DoAr 21. This strong radiation may also have played a role in removing any disk from around DoAr 21, despite its young age.

REFERENCES

Alexander, R. D., Clarke, C. J., & Pringle, J. E. 2005, MNRAS, 358, 283

Allamandola, L. J., Hudgins, D. M., & Sandford, S. A. 1999, ApJ, 511, L115

Aller, L. H., et al. 1982, Landolt-Bornstein: Numerical Data and Functional Relationships in Science and Technology,

Allers, K. N., Jaffe, D. T., Lacy, J. H., Draine, B. T., & Richter, M. J. 2005, ApJ, 630, 368

Anders, E. & Grevesse, N. 1989, *Geochim Cosm. Acta*, 53, 197

André, P., Montmerle, T., Feigelson, E. D., & Steppe, H. 1990, A&A, 240, 321

André, P., Deeney, B. D., Phillips, R. B., & Lestrade, J. 1992, ApJ, 401, 667

Argiroffi, C., Drake, J. J., Maggio, A., Peres, G., Sciortino, S., & Harnden, F. R. 2004, ApJ, 609, 925

Aufdenberg, J. P., Hauschildt, P. H., & Baron, E. 1999, MNRAS, 302, 599

Bary, J. S., Weintraub, D. A., & Kastner, J. H. 2002, ApJ, 576, L73

Bary, J. S., Weintraub, D. A., & Kastner, J. H. 2003, ApJ, 586, 1136

Bary, J. S., Weintraub, D. A., Shukla, S. J., Leisenring, J. M., & Kastner, J. H. 2008, ApJ, 678, 1088

Beck, T. L., McGregor, P. J., Takami, M., & Pyo, T.-S. 2008, ApJ, 676, 472

Bitner, M. A., et al. 2008, ApJ, 688, 1326

Blumenthal G.R., Drake G.W.F., Tucker W.H., 1972, ApJ, 172, 205

Bontemps, S., et al. 2001, A&A, 372, 173

Boulanger, F., et al. 2005, A&A, 436, 1151

Bouvier, J. & Appenzeller, I. 1992, A&AS, 92, 481

Bouvier, J., Bertout, C., & Bouchet, P. 1988, A&AS, 75, 1

Buser, R., & Kurucz, R. L. 1992, A&A, 264, 557

Canizares C.R., et al., 2005, PASP, 117, 1144

Casanova, S., Montmerle, T., Feigelson, E. D., & Andre, P. 1995, ApJ, 439, 752

Cash, W. 1979, ApJ, 228, 939

Chapman, N. L., Mundy, L. G., Lai, S.-P., & Evans, N. J., II 2008, arXiv:0809.1106

Cieza, L., et al. 2007, ApJ, 667, 308

Cieza, L. A., Swift, J. J., Mathews, G. S., & Williams, J. P. 2008, ApJ, 686, L115

Cohen, M., Walker, R. G., Carter, B., Hammersley, P., Kidger, M., & Noguchi, K. 1999, AJ, 117, 1864

D'Antona, F., & Mazzitelli, I. 1997, Memorie della Societa Astronomica Italiana, 68, 807

Dolidze, M. V. & Arakelyan, M. A. 1959, Soviet Ast., 3, 434

Draine, B. T. 2003, ARA&A, 41, 241

Favata, F., Micela, G., & Sciortino, S. 1998, A&A, 337, 413

Feigelson, E. D. & Montmerle, T. 1985, ApJ, 289, 19

Feigelson, E. D. & Montmerle, T. 1999, ARA&A, 37, 363

Feigelson, E. D., Garmire, G. P., & Pravdo, S. H. 2002, ApJ, 572, 335

Fernández, M., et al. 2004, A&A, 427, 263

Flaccomio, E., Damiani, F., Micela, G., Sciortino, S., Harnden, F. R., Jr., Murray, S. S., & Wolk, S. J. 2003, ApJ, 582, 398

Furlan, E., et al. 2006, ApJS, 165, 568

Gabriel, A. H., & Jordan, C. 1969, MNRAS, 145, 241

Gagné M., Skinner S. L., Daniel K. J., 2004, ApJ, 613, 393

Galliano, F., Madden, S. C., Tielens, A. G. G. M., Peeters, E., & Jones, A. P. 2008, ApJ, 679, 310

Geers, V. C., et al. 2006, A&A, 459, 545

Gómez, M., Stark, D. P., Whitney, B. A., & Churchwell, E. 2003, AJ, 126, 863

Güdel M., Telleschi A., 2007, A&A, 474, 25

Habart, E., Boulanger, F., Verstraete, L., Pineau des Forêts, G., Falgarone, E., & Abergel, A. 2003, A&A, 397, 623

Habing, H. J. 1968, Bull. Astron. Inst. Netherlands, 19, 421

Hanner, M. S., Brooke, T. Y., & Tokunaga, A. T. 1995, ApJ, 438, 250

Haro, G. 1949, AJ, 54, 188

Herczeg, G. J., Linsky, J. L., Walter, F. M., Gahm, G. F., & Johns-Krull, C. M. 2006, ApJS, 165, 256

Hidajat, B. 1961, Contributions from the Bosscha Observatory, 11, 1

Hony, S., Van Kerckhoven, C., Peeters, E., Tielens, A. G. G. M., Hudgins, D. M., & Allamandola, L. J. 2001, A&A, 370, 1030

Houck, J. C., & Denicola, L. A. 2000, Astronomical Data Analysis Software and Systems IX, 216, 591

Igea, J. & Glassgold, A. E. 1999, ApJ, 518, 848

Imanishi K., Tsujimoto M., Koyama K., 2002, ApJ, 572, 300

Itoh, Y., Sugitani, K., Ogura, K., & Tamura, M. 2003, PASJ, 55, L77

Jensen, E. L. N., Mathieu, R. D., Donar, A. X., & Dullighan, A. 2004, ApJ, 600, 789

Joblin, C., Tielens, A. G. G. M., Geballe, T. R., & Wooden, D. H. 1996, ApJ, 460, L119

Kastner, J. H., Huenemoerder, D. P., Schulz, N. S., Canizares, C. R., & Weintraub, D. A. 2002, ApJ, 567, 434

Kastner, J. H., Huenemoerder, D. P., Schulz, N. S., Canizares, C. R., Li, Jingqiang, & Weintraub, D. A. 2004, ApJ, 605, 49

Keenan, P. C., & McNeil, R. C. 1989, ApJS, 71, 245

Koerner, D. W., Jensen, E. L. N., Cruz, K. L., Guild, T. B., & Gultekin, K. 2000, ApJ, 533, L37

Koyama, Katsuji, Maeda, Yoshitomo, Ozaki, Masanobu, Ueno, Shiro, Kamata, Yuichi, Tawara, Yuzuru, Skinner, Stephen, & Yamauchi, Shigeo 1994, PASJ, 46, 125

Kundurthy, P., Meyer, M. R., Robberto, M., Beckwith, S. V. W., & Herbst, T. 2006, AJ, 132, 2469

Massarotti, A., Latham, D. W., Torres, G., Brown, R. A., & Oppenheimer, B. D. 2005, AJ, 129, 2294

Lada, C. J. & Wilking, B. A. 1984, ApJ, 287, 610

Liseau, R., et al. 1999, A&A, 344, 342

Loinard, L., Torres, R. M., Mioduszewski, A. J., & Rodríguez, L. F. 2008, ApJ, 675, L29

Luhman, K. L. & Rieke, G. H. 1999, ApJ, 525, 440

MacFarlane, J. J., Golovkin, I. E., Woodruff, P. R., Welch, D. R., Oliver, B. V., Mehlhorn, T. A., Campbell, R. B. 2004, in *Proceedings of the Third Conference on Intertial Fusion Science and Applications*, B. A. Hammel, D. D. Meyerhofer, J. M. ter Vehn, & H. Azechi, eds., Am. Nucl. Soc.

Maloney, P. R., Hollenbach, D. J., & Tielens, A. G. G. M. 1996, ApJ, 466, 561.

Martín, E. L., Montmerle, T., Gregorio-Hetem, J., & Casanova, S. 1998, MNRAS, 300, 733

Martin, P. G., et al. 1992, ApJ, 392, 691

McClure, M. K. 2008, arXiv:0810.4561

Montes, D., Fernandez-Figueroa, M. J., de Castro, E., & Sanz-Forcada, J. 1997, A&AS, 125, 263

Montmerle, T., Koch-Miramond, L., Falgarone, E., & Grindlay, J. E. 1983, ApJ, 269, 182

Morrison R., McCammon D., 1983, ApJ, 270, 119

Najita, J., Carr, J. S., & Mathieu, R. D. 2003, ApJ, 589, 931

Nomura, H., & Millar, T. J. 2005, A&A, 438, 923

Nomura, H., Aikawa, Y., Tsujimoto, M., Nakagawa, Y., & Millar, T. J. 2007, ApJ, 661, 334

Okumura, K., Pérault, M., & Longval, Y. 1998, technical report, Ghosts in ISOCAM images (http://www.iso.vilspa.esa.es/users/expl_lib/CAM_list.html)

Padgett, D. L., et al. 2008, ApJ, 672, 1013

Palla, F., & Stahler, S. W. 1999, ApJ, 525, 772

Phillips, R. B., Lonsdale, C. J., & Feigelson, E. D. 1991, ApJ, 382, 261

Porquet D.,Dubau J., 2000, A&AS, 143, 495

Preibisch, T. 1999, A&A, 345, 583

Puget, J. L., & Leger, A. 1989, ARA&A, 27, 161

Ramsay Howat, S. K., & Greaves, J. S. 2007, MNRAS, 379, 1658

Román-Zúñiga, C. G., Lada, C. J., Muench, A., & Alves, J. F. 2007, ApJ, 664, 357

Rydgren, A. E., Strom, S. E., & Strom, K. M. 1976, ApJS, 30, 307

Rydgren, A. E., & Vrba, F. J. 1983, ApJ, 267, 191

Sanz-Forcada, J., Maggio, A., & Micela, G. 2003, A&A, 408, 1087

Schmitt, J. H. M. M., Robrade, J., Ness, J.-U., Favata, F., & Stelzer, B. 2005, A&A, 432, L35

Sellgren, K., Uchida, K. I., & Werner, M. W. 2007, ApJ, 659, 1338

Siess, L., Dufour, E., & Forestini, M. 2000, A&A, 358, 593

Smith R. K., Brickhouse N. S., Liedahl D. A., Raymond J. C., 2001, ApJ, 556, L91

Stapelfeldt, K. R., et al. 2009, in preparation

Stelzer, B. & Schmitt, J. H. M. M. 2004, A&A, 418, 687

Stine, P. C., Feigelson, E. D., Andre, P., & Montmerle, T. 1988, AJ, 96, 1394

Takami, M., Chrysostomou, A., Ray, T. P., Davis, C., Dent, W. R. F., Bailey, J., Tamura, M., & Terada, H. 2004, A&A, 416, 213

Telleschi, A., Güdel, M., Briggs, K. R., Audard, M., & Scelsi, L. 2007, A&A, 468, 443

Tielens, A. G. G. M. 2008, ARA&A, 46, 289

Torres, R. M., Loinard, L., Mioduszewski, A. J., & Rodríguez, L. F. 2007, ApJ, 671, 1813

Valenti, J. A., Basri, G., & Johns, C. M. 1993, AJ, 106, 2024

Valenti, J. A., Fallon, A. A., & Johns-Krull, C. M. 2003, ApJS, 147, 305

Vrba, F. J., Coyne, G. V., & Tapia, S. 1993, AJ, 105, 1010

Vuong, M. H., Montmerle, T., Grosso, N., Feigelson, E. D., Verstraete, L., & Ozawa, H. 2003, A&A, 408, 581

Weingartner, J. C., & Draine, B. T. 2001a, ApJ, 548, 296

Weingartner, J. C., & Draine, B. T. 2001b, ApJS, 134, 263

Weintraub, D. A., Saumon, D., Kastner, J. H., & Forveille, T. 2000, ApJ, 530, 867

White, R. J., & Basri, G. 2003, ApJ, 582, 1109

White, R. J., & Ghez, A. M. 2001, ApJ, 556, 265

Wilking, B. A., Schwartz, R. D., & Blackwell, J. H. 1987, AJ, 94, 106

Wilking, B., Gagné, M., & Allen, L. 2008, in Handbook of Star Forming Regions, Vol. 2, ed.
 B. Reipurth (San Francisco: ASP), pp. 351–380; arXiv:0811.0005